



Article

Fractal-Based Pattern Quantification of Mineral Grains: A Case Study of Yichun Rare-Metal Granite

Yue Liu ^{1,†}, Tao Sun ^{1,*,†} , Kaixing Wu ^{1,2,*}, Hongwei Zhang ¹, Jingwei Zhang ¹, Xinwen Jiang ¹, Quanwei Lin ¹ and Mei Feng ¹

¹ School of Resources and Environmental Engineering, Jiangxi University of Science and Technology, Ganzhou 341000, China

² Jiangxi Key Laboratory of Mining Engineering, Jiangxi University of Science and Technology, Ganzhou 341000, China

* Correspondence: suntao@jxust.edu.cn (T.S.); wukaixing@jxust.edu.cn (K.W.); Tel.: +86-0797-831-2751 (T.S.)

† These authors contributed equally to this work.

Abstract: The quantification of the irregular morphology and distribution pattern of mineral grains is an essential but challenging task in ore-related mineralogical research, allowing for tracing the footprints of pattern-forming geological processes that are crucial to understanding mineralization and/or diagenetic systems. In this study, a large model, namely, the Segmenting Anything Model (SAM), was employed to automatically segment and annotate quartz, lepidolite and albite grains derived from Yichun rare-metal granite (YCRMG), based on which a series of fractal and multifractal methods, including box-counting calculation, perimeter–area analysis and multifractal spectra, were implemented. The results indicate that the mineral grains from YCRMG show great scaling invariance within the range of 1.04–52,300 μm . The automatic annotation of mineral grains from photomicrographs yields accurate fractal dimensions with an error of only 0.6% and thus can be utilized for efficient fractal-based grain quantification. The resultant fractal dimensions display a distinct distribution pattern in the diagram of box-counting fractal dimension (D_b) versus perimeter–area fractal dimension (D_{PA}), in which lepidolites are sandwiched between greater-valued quartz and lower-valued albites. Snowball-textured albites, i.e., concentrically arranged albite laths in quartz and K-feldspar, exhibit characteristic D_b values ranging from 1.6 to 1.7, which coincide with the fractal indices derived from the fractal growth model. The zonal albites exhibit a strictly increasing trend regarding the values of fractal and multifractal exponents from core to rim, forming a featured “fractal-index banding” in the radar diagram. This pattern suggests that the snowball texture gradually evolved from rim to core, thus leading to greater fractal indices of outer zones, which represent higher complexity and maturity of the evolving system, which supports a metasomatic origin of the snowball texture. Our study demonstrates that fractal analyses with the aid of a large model are effective and efficient in characterizing and understanding complex patterns of mineral grains.

Keywords: fractal; pattern quantification; large model; SAM; mineral grain; Yichun rare-metal granite



Citation: Liu, Y.; Sun, T.; Wu, K.; Zhang, H.; Zhang, J.; Jiang, X.; Lin, Q.; Feng, M. Fractal-Based Pattern Quantification of Mineral Grains: A Case Study of Yichun Rare-Metal Granite. *Fractal Fract.* **2024**, *8*, 49. <https://doi.org/10.3390/fractalfract8010049>

Academic Editors: Carlo Cattani and Erick Ogam

Received: 15 November 2023

Revised: 15 December 2023

Accepted: 9 January 2024

Published: 12 January 2024



Copyright: © 2024 by the authors. Licensee MDPI, Basel, Switzerland. This article is an open access article distributed under the terms and conditions of the Creative Commons Attribution (CC BY) license (<https://creativecommons.org/licenses/by/4.0/>).

1. Introduction

Fractal geometry provides a powerful mathematical tool for scientific research on natural phenomena with complex morphological features [1], which allows for effectively revealing complex patterns in chaotic and irregular natural structures along with their underlying nonlinear dynamic processes [2]. Over the past several decades, fractal/multifractal theory has achieved outstanding advancements in quantitatively characterizing complex structures or phenomena in various fields of geoscience from macro- to micro-scales, including the following: (a) At a global to provincial scale, the occurrences of giant geological systems, such as earthquake systems, tectonic systems and metallogenic provinces, are often characterized by spatial- and/or temporal-domain statistical scaling laws, which can be

portrayed by diverse fractal dimensions [3–7]. (b) At a regional to deposit scale, fractal analysis is widely utilized as a quantitative means to characterize the intricate distributions of ore-forming systems [8–12], i.e., exploring the correlation between mineralization and ore-related spatial–temporal structures through fractal exponents and searching for mineralization patterns [13–16]. The most prominent achievement in this field is the effective decomposition of geochemical populations using a variety of fractal models [17–26], including concentration–area fractal model [19–21], concentration–distance fractal model [22], concentration–volume fractal model [23], spectrum–area multifractal model [24] and singularity indices [25,26]. (c) At a microscopic scale, fractal dimensions derived from various fractal/multifractal analyses, such as the box-counting model, perimeter–area model and number–area model [13,27–29], have been employed to quantify the irregularities in the shape and distribution pattern of mineral grains.

Fractal and multifractal methods have been shown to be effective in delineating diverse complex geological patterns, as mentioned above; however, most studies have focused on recognizable macroscopic geometries, such as structures, geophysical and geochemical anomalies, and ore-related evidence, while only a few contributions have employed fractal analyses for mineral pattern characterization at the microscopic scale. Notably, mineralogical research has long been considered fundamental for ore-forming systems, while fractal-derived indices are quite suitable for characterizing the main targets of mineralogical studies, including but not limited to morphological descriptions [30], micro-structures [31], compositional variance [32,33], special textures [29] and mineral staging [13]. The microscopic information extracted from these fractal indices and their underlying scaling properties of mineral patterns can be utilized to trace the footprints of pattern-forming geological processes, which are crucial to understanding mineralization and/or diagenetic systems [34,35].

Despite its great significance, fractal-based mineral pattern analyses are still rarely reported because of the challenging image-processing procedure. This is mainly due to the fact that considerable manual interventions and labeling are inevitably needed to annotate microscopic mineral grains from digital images of rock plates and thin sections. Such work is quite time-consuming and may sometimes be inaccurate and subjective in the current framework of image processing, since mineral grains in some rocks are difficult to distinguish. Most recently, benefiting from the rapid development of machine learning techniques, large models, represented by Chat Generative Pre-trained Transformer (ChatGPT), have sparked a revolution in industrial and academic fields [36–38]. With the aid of a large model, highly intelligent image segmentation and annotation of microscopic objects, such as minerals, have become available [39,40], which provides a promising solution to the above-mentioned issue.

The aims of this paper are (1) to probe a feasible scenario for efficient annotation of mineral images that can build a solid foundation for subsequent fractal analyses at the microscopic scale; (2) to construct a quantitative framework for characterizing the morphological features and distribution patterns of mineral grains; and (3) to trace the proxy of pattern-forming processes of target minerals using fractal analyses. Yichun rare-metal granite (YCRMG), which originated in the famous Yichun Ta-Nb deposit, is chosen as a case study, since it is well known for its characteristic mineral compositions and textures, which are deemed special products of highly evolved granite magma [41]. A large model referred to as Segmenting Anything Model (SAM) was introduced in this study to process digital images and extract mineral grains, based on which fractal and multifractal analyses were implemented. The results contribute to quantifying the irregular geometries and distribution patterns of mineral grains and provide some clues for the controversial issue of mineral origin.

2. Study Area and Data Used

The Yichun Ta-Nb deposit, which is situated in the northern part of the Cathaysia Block in southeast China, is the largest Ta producer in China, with an original Ta reserve greater

than 11 kt [42]. Economic Ta-Nb mineralization is disseminated throughout YCRMG. YCRMG occurs as a thin sheet confined to the uppermost part of the Yashan granitic complex (Figure 1), which is supposed to be magmatic and to have intruded into Lower Proterozoic metasediments during the early Yanshanian granite-forming event in South China, covering an outcrop area of approximately 9.5 km² [43,44] (Figure 1). The granitic complex is supposed to consist of multi-stage intrusive units that exhibit distinct vertical zonation in the cross section, including mainly protolithionite–muscovite granite, Li-mica granite and topaz–lepidolite granite from the bottom to the top (Figure 1b).

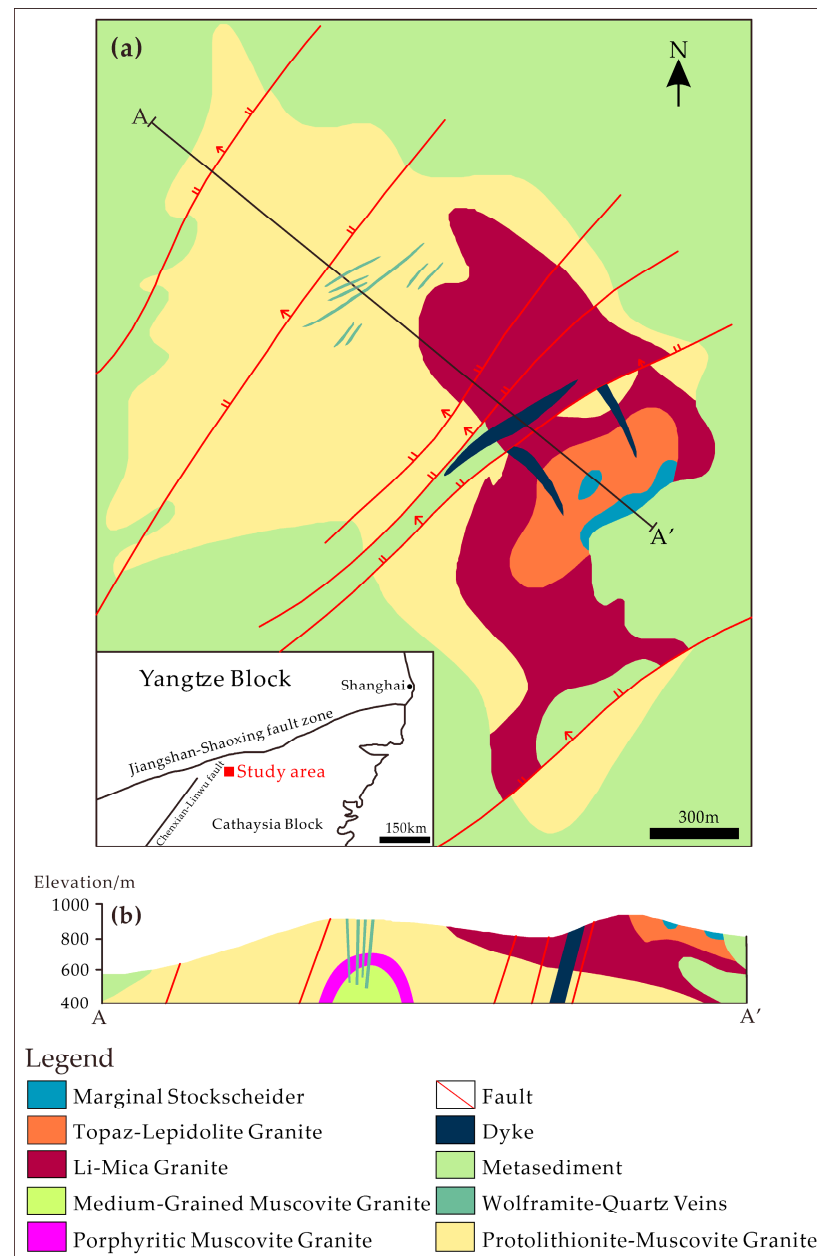


Figure 1. Simplified geological map (a) and typical cross section (b) of YCRMG, modified from [42,44,45].

YCRMG is composed dominantly of quartz, lepidolite and albite (Figure 2a–c), with minor topaz, K-feldspar, amblygonite and accessory monazite, columbite–tantalite, microcline and Ta-rich cassiterite [43]. The rocks are “porphyritic like” and contain “phenocrysts” up to 10 mm of quartz (~20–25%), K-feldspar (<5%) and topaz (<2%), as well as fine-grained

groundmass consisting mainly of albite (~40–60%) and lepidolite crystals (~15–30%) [43,45]. It can be commonly observed that albite laths are concentrically arranged along the growth zones of anhedral–subhedral “phenocrysts” of quartz or K-feldspar (Figure 2d), which is generally referred to as “snowball” texture [43–46].

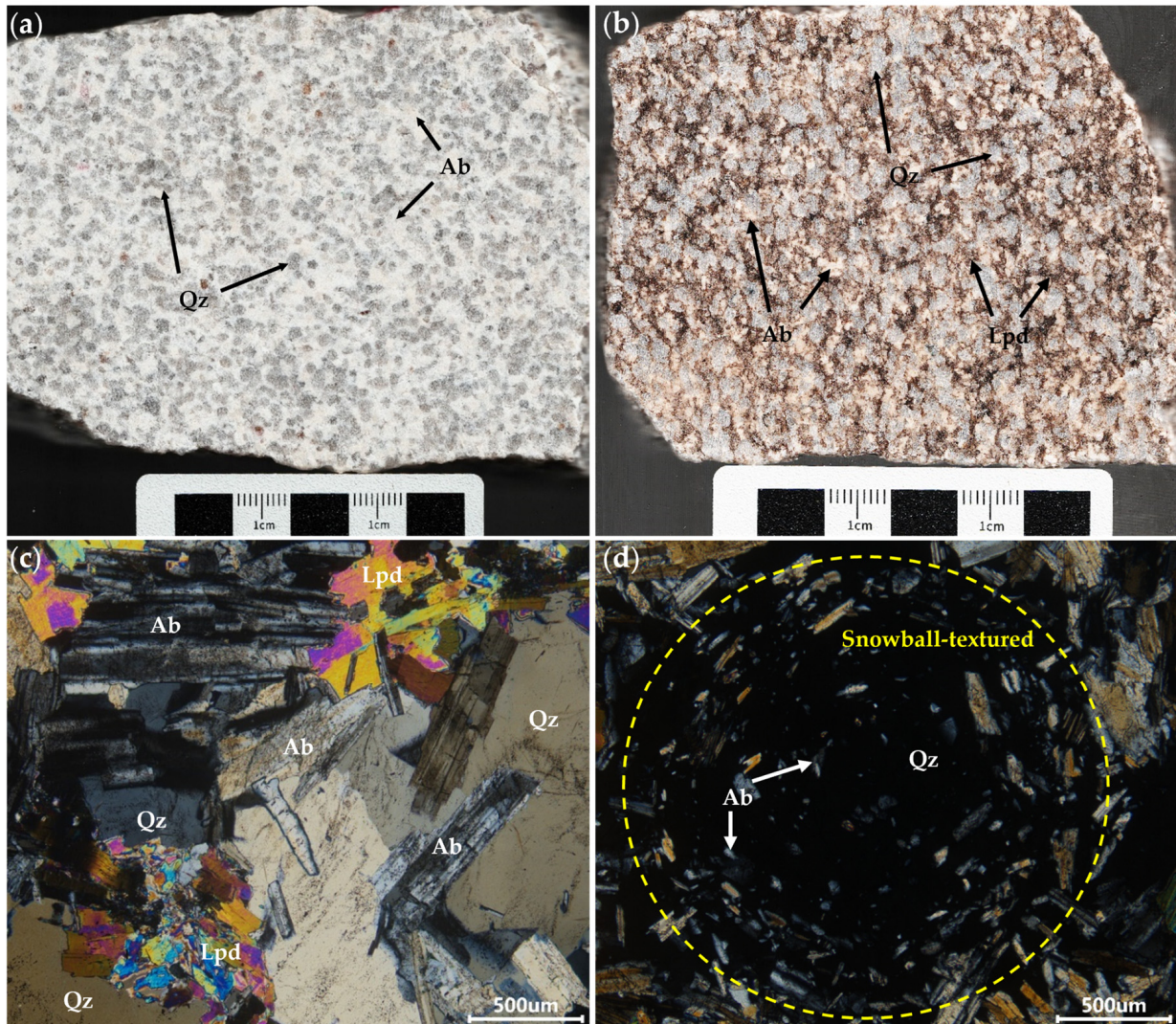


Figure 2. (a) Scanned image of the polished surface of a hand specimen showing albites and snowball-textured quartz. (b) Scanned image of the polished surface of a hand specimen showing the three main minerals of YCRMG. (c) Photomicrograph showing the three main minerals of YCRMG. (d) Photomicrograph of a representative snowball-textured quartz containing concentrically zoned albite inclusions. Abbreviations: Ab = albite, Lpd = lepidolite, Qz = quartz.

Fifty-six hand specimens were sampled from YCRMG in the Yashan granitic complex. These specimens were then polished and prepared into thin sections. The polished surfaces of the specimens were scanned with a commercial light scanner with an optical resolution of 3400×2700 pixels. The thin sections were observed and imaged with a Leica DM2700 P polarization microscope, which can output photomicrographs with a resolution of 2448×2048 pixels (Figure 2c,d). A total of 17 digital images representative of major minerals of the granite complex, including 2 scanned images of polished hand specimens (Figure 2a,b) and 15 photomicrographs of quartz, lepidolites and albites (Figure 3), were selected for the following fractal analyses.

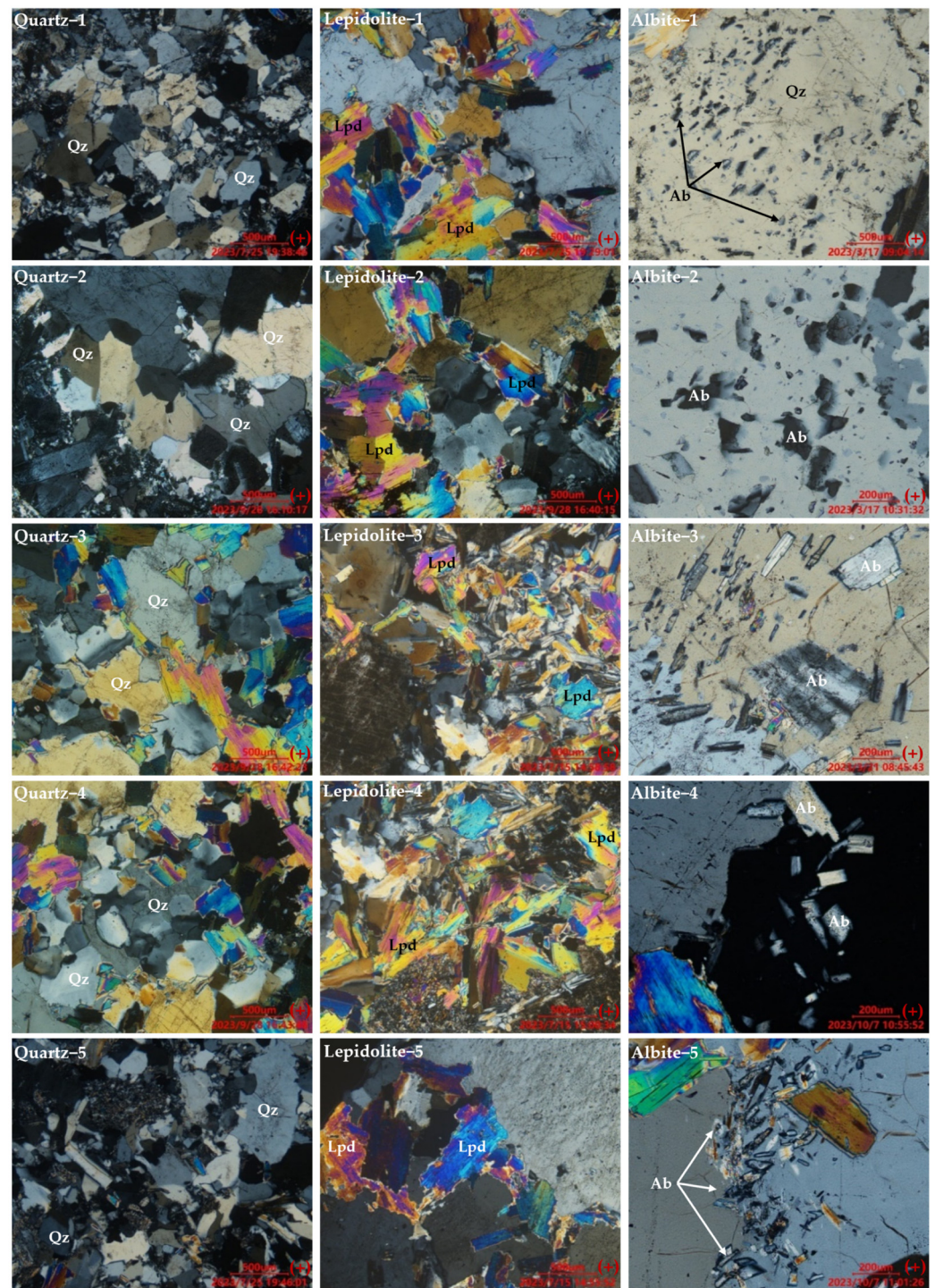


Figure 3. Photomicrographs of representative rock-forming minerals from YCRMG. Abbreviations: Ab = albite, Lpd = lepidolite, Qz = quartz.

3. Methods

3.1. Image Annotation

Large models aim to train large-scale and self-supervised models based on big data [36,47]. In particular, the emergence of ChatGPT has resulted in substantial changes in the field of artificial intelligence (AI) [37]. Motivated by the success of ChatGPT, the SAM, a new AI model from Meta AI, provides a promotable segmentation system with zero-shot generalization, facilitating the segmentation of unfamiliar objects and images without the need for additional training [39,48]. The SAM has been trained on more than 1 billion masks derived

from 11 million images and shows the ability to apply prompt engineering and resolve various downstream segmentation tasks on new data distributions. The breakthrough achieved by the SAM simplifies the necessity of executing numerous labeling, stacking and arithmetically power-consuming algorithms in an image-processing task [39,47].

In this study, an SAM-based image annotation procedure is introduced to process a variety of mineral photomicrographs. The original photomicrographs and object membership labels are provided as input. After being processed by an image encoder, a prompt encoder and a mask decoder, masks are generated to indicate the region of the image that corresponds to the constraints. Such constraints can be well specified by the input prompts based on the provided points or bounding boxes [39,49] (Figure 4).

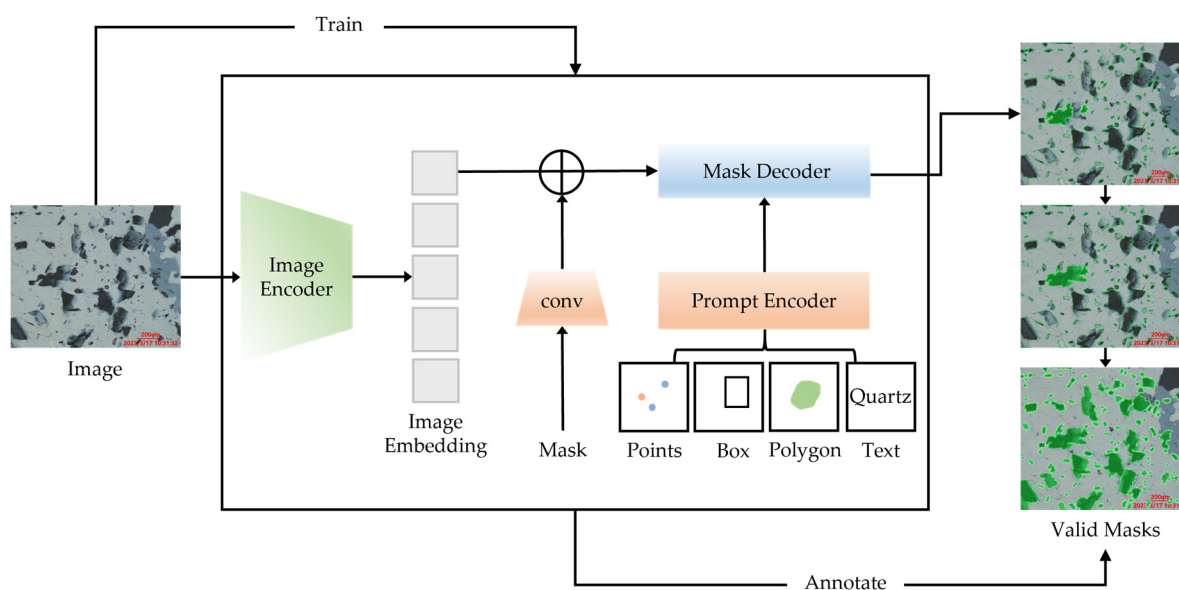


Figure 4. Flowchart of image annotation using the SAM, modified from [39,40].

The image encoder utilizes a visual transformer that is pre-trained with the masking strategy of a masking automatic encoder [50,51]. Its functions include encoding photomicrographs into vectors; generating image embeddings; and mapping high-dimensional images to a low-dimensional characteristic space (Figure 4), which handles high-resolution inputs with minimum adaptation. The prompt encoder tackles various forms of sparse prompts (points, boxes or sentences) and dense prompts (masks) through several branches of a fundamental convolutional neural network (Figure 4). Dense prompts (masks) of photomicrographs, i.e., mineral grain regions, exhibit a spatial correlation with the image, which can then be efficiently queried by input prompts to produce object masks at amortized, real-time speeds [39] (Figure 4). Subsequently, the mask decoder is trained to map the causal relationship between the given embeddings and the associated masks. The algorithm employs prompt self-attention and cross-attention mechanisms from the transformer to update all the embeddings [52], facilitating the interaction between feature maps and prompts [40] (Figure 4). The open-source code for image segmentation with the SAM is accessible at <https://github.com/facebookresearch/segment-anything> on 15 December 2023. The pseudo code describing the implementation of SAM-based image segmentation is listed in Algorithm 1.

The SAM generates segmentation results for unknown classes without additional training, owing to its great generalization capability. However, it is necessary to assign labels to these segmented objects (i.e., quartz, lepidolite and albite) for the subsequent image processing and fractal analysis. For that, we employed an automatic image annotation tool referred to as AnyLabeling, which integrates the SAM for assigning labels to segmentation masks for the target mineral types [53,54]. The open-source code is accessible at <https://github.com/vietanhdev/anylabeling>.

Algorithm 1: The SAM for mineral photomicrograph image segmentation

Input: Image dataset I , image prompt of classes C (quartz, lepidolite, albite), flag indicating whether to generate multiple masks or a single mask *Multimask*.

Output: Predicted mask set M .

Initialize image mask m

for i in I do

$image_tensor \leftarrow preprocess(i)$

$prompt_encoding \leftarrow prompt_encoder(C)$

$image_embedding \leftarrow image_encoder(image_tensor)$

$mask_prediction \leftarrow mask_decoder(image_embedding, prompt_encoding)$

 if *multimask* is True then

$m \leftarrow multiple.mask_prediction$

 else

$m \leftarrow single.mask_prediction$

 end if

$M.append(m)$

end

The automatically annotated photomicrograph dataset was processed with image binarization utilizing the Python programming language [55,56], which allows for a clear visual effect with a binary color scheme of black and white. Instead of identifying objects, the binarization process separates the target mineral grains from the background [57–59]. Subsequently, each pixel in the automatically annotated photomicrograph exhibits only one of the following two values: 255 (white) or 0 (black), which represent the target mineral space and background matrix, respectively (Figure 5b).

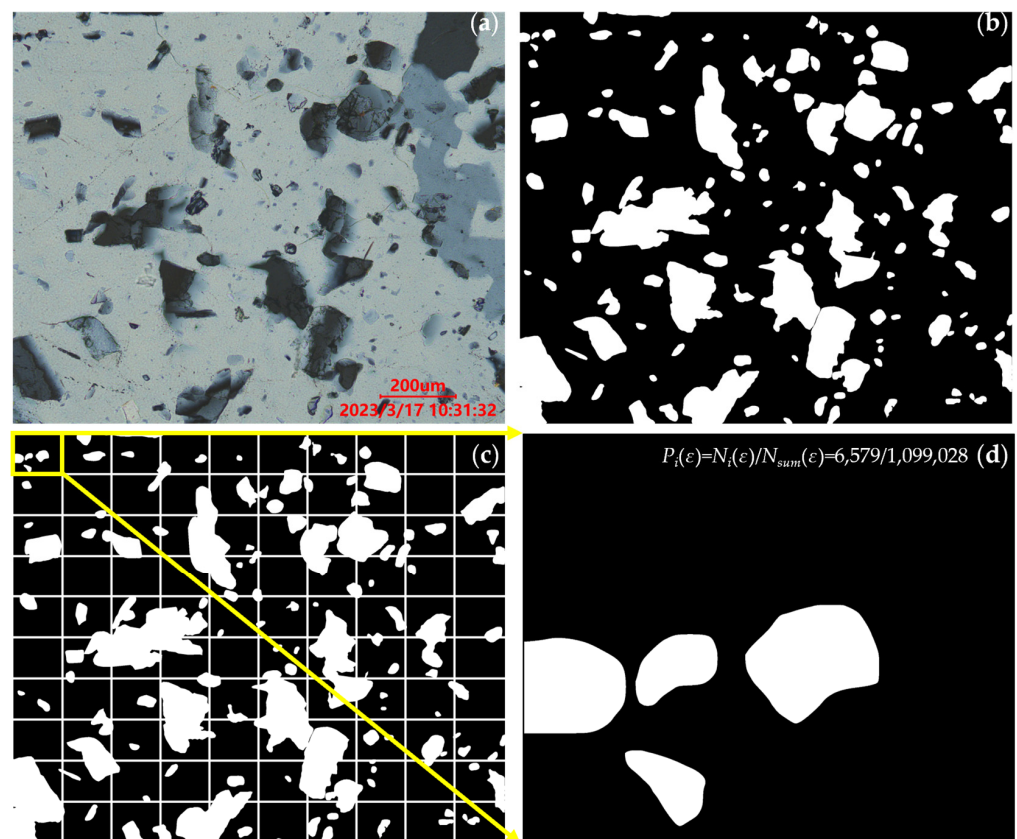


Figure 5. Calculating process of the probability mass function. (a) Photomicrograph of a representative texture of albite. (b) Annotated result of albite grains. (c) Subdivision of annotated image by a number of boxes with a size of ϵ pixels. (d) Calculation of the probability mass function in the i th box.

3.2. Box-Counting Fractal Method

Fractals were first introduced to the natural sciences by Mandelbrot in the 1970s. They aim to characterize unsmooth and irregular geometries occurring in nature and nonlinear systems, which are basically characterized by self-similarity or scale invariance [1,2].

The box-counting method is a commonly employed approach for calculating the fractal dimension of irregular shapes. The result of box counting, which is referred to as box-counting dimension (D_b), is defined by the following formula [60,61]:

$$D_b = -\lim_{r \rightarrow 0} \frac{\lg N(r)}{\lg r}, \quad (1)$$

where r is the box size and $N(r)$ is the counted number of boxes of length r needed to cover target fractal geometries.

In this study, the annotated photomicrographs were divided into a grid of boxes with size r , and the number of those boxes containing at least one pixel of target mineral was counted and denoted as $N(r)$. The box size progressively varied, and the corresponding $N(r)$ was counted. A set of point pairs of $(N(r), r)$ were then projected in a double logarithmic diagram, in which a fitting line was drawn using the least square method. The box-counting fractal dimension can be obtained from the slope of the fitting line [30].

3.3. Perimeter–Area Fractal Model

The perimeter–area model, initially developed by Mandelbrot, is commonly employed to represent the power-law relationship between the perimeter and the area of similarly shaped fractals in two-dimensional space [2,62,63], which is formulized as [19]

$$P \propto A^{\frac{1}{2}D_{PA}}, \quad (2)$$

where P is the perimeter of each annotated mineral grain, A is the area of the corresponding grain and D_{PA} denotes the perimeter–area fractal dimension [13,28,29].

In a practical D_{PA} calculation procedure, the annotated photomicrographs are converted into vector format (Figure 6a) and then imported into ArcGIS 10.2 to calculate the perimeter and area of each mineral grain (Figure 6b,c). The data pairs of P and A are then projected to a log–log plot, where the projected points can be fitted by a regression line using the least square method [18] (Figure 6d). D_{PA} is estimated by doubling the slope of the regression line according to the following formula [19]:

$$\text{Log}(P) = C + \frac{1}{2}D_{PA}\text{log}(A) \quad (3)$$

where C is a constant. D_{PA} is an effective coefficient for characterizing the irregularities of areal geometries [64].

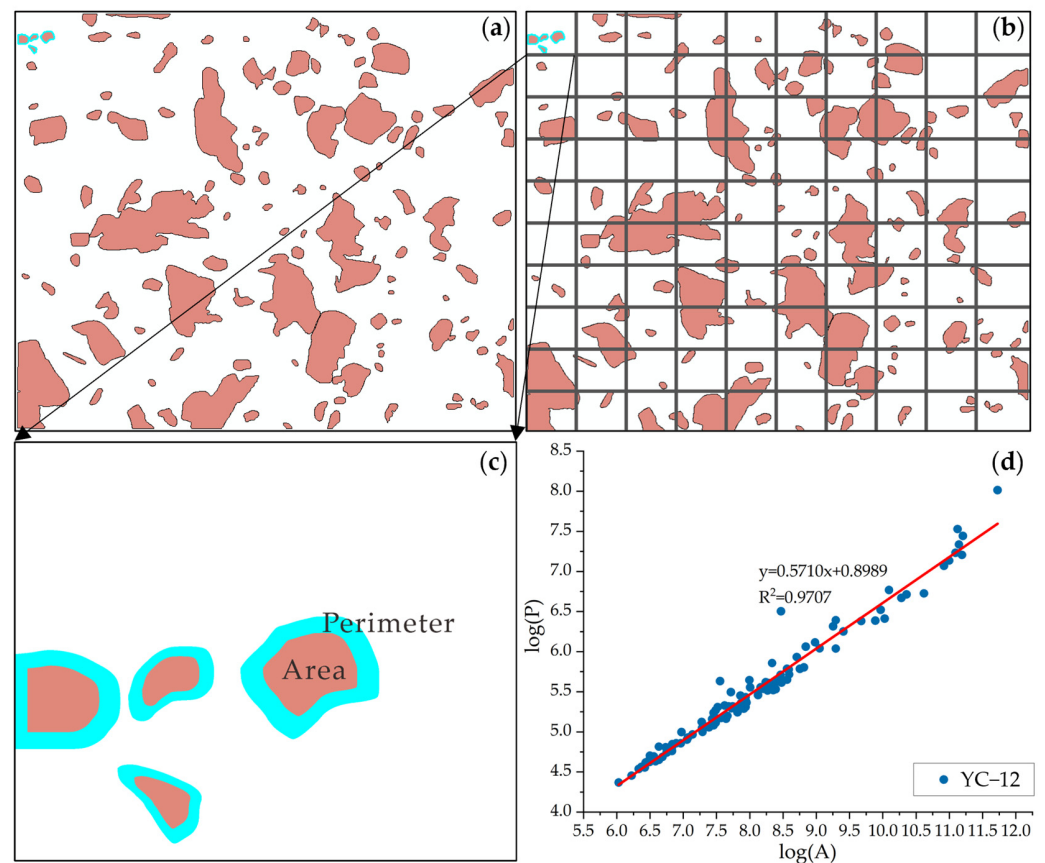


Figure 6. Calculating process of the perimeter–area fractal model. (a) Vectograph of mineral grains converted from annotated image. (b) Subdivision of vectograph by a number of boxes with a size of ε pixels. (c) Measurement of the perimeter and area of each mineral grain in the vectograph. (d) Projection of perimeter (P) and area (A) in a log–log plot for estimating D_{PA} by doubling the slope of the fitting line.

3.4. Multifractal Method

Multifractal theory is regarded as an extension of fractal theory and requires a spectrum of fractal dimensions, i.e., the multifractal spectrum, to characterize the multifractal features [2,65]. In comparison, fractal is used mainly to describe irregular geometric forms and sets, while multifractal is used to describe the normalized probability distributions over a range of different measures. Multifractal measures can be calculated with a statistical physical moment method [66–68], which is fundamental for practical multifractal analyses of spatial data and images.

The annotated photomicrographs were divided into a certain number of boxes with a size of ε pixels (Figure 5c). The probability mass function in the i th box is expressed as [66]

$$P_i(\varepsilon) = \frac{N_i(\varepsilon)}{N_{sum}(\varepsilon)}, \quad (4)$$

where $N_i(\varepsilon)$ is the counted number of annotated mineral pixels in the i th box of scale ε and $N_{sum}(\varepsilon)$ is the total number of annotated mineral pixels within all boxes (Figure 5d).

In the case of minerals with multifractal characteristics, $P_i(\varepsilon)$ is equivalently described by a probability distribution that scales with different exponents for each box size ε [2]:

$$P_i(\varepsilon) \propto \varepsilon^{\alpha_i}, \quad (5)$$

where α_i is the Lipschitz–Hölder exponent, namely, the singularity index.

$N_\alpha(\varepsilon)$ is defined as an evaluation of the number of boxes that have a specific singularity strength α , which is formulized as [2,69]

$$N_\alpha(\varepsilon) \propto \varepsilon^{-f(\alpha)}, \tag{6}$$

where $f(\alpha)$ is the spectral function of fractal dimensions that describes the abundance of the set of boxes with α .

The partition function, χ_q , is a foundational quantity and is expressed as follows [2,66]:

$$\chi_q(\varepsilon) = \sum_{i=1}^n p_i^q(\varepsilon), q \in R, \tag{7}$$

where q is the moment of the weighted sum and n is the number of boxes that constitute the sampling space.

In practice, the mass exponent function, $\tau(q)$, is initially estimated from $\chi_q(\varepsilon)$. $\tau(q)$ describes the local density of the fractal ensemble, which is formulized as [70]

$$\tau(q) = \lim_{\varepsilon \rightarrow 0} \frac{\log \chi_q(\varepsilon)}{\log(\varepsilon)} = \lim_{\varepsilon \rightarrow 0} \frac{\log \left(\sum_{i=1}^n p_i^q(\varepsilon) \right)}{\log(\varepsilon)} \tag{8}$$

The total number of pixels in the mineral region of the i th box is measured as $P_i(\varepsilon)$. With different q , $\chi_q(\varepsilon)$ has a simple power-law relationship with the box of size, ε [2,65]:

$$\chi_q(\varepsilon) \propto \varepsilon^{\tau(q)}, \tag{9}$$

where $\tau(q)$ is the power exponent of the q th-order moment. An apparent linear relationship exists between χ_q and ε in a log–log diagram, based on which $\tau(q)$ can be estimated from the slope of the fitting line at a specific q (Figure 7b). The generalized fractal dimension (D_q) is derived from $\tau(q)$, which is formulized as follows [69,71]:

$$D_q = \begin{cases} \tau(q)/1 - q, q \neq 1 \\ -\tau'(q), q = 1 \end{cases} \tag{10}$$

The generalized fractal dimension explains the scaling behaviors of a multifractal set [72,73], where D_q is the fractal dimension of the moment order (q) (Figure 7c). With $q = 1$ and 2, the corresponding D_1 and D_2 denote the information dimension and correlation dimension, respectively [74].

Equations (5), (6) and (9) are combined as [2,65]

$$\chi_q(\varepsilon) = \int \varepsilon^{q\alpha - f(\alpha)} d\alpha, \tag{11}$$

If $\tau(q)$ is a smooth function of q , $\alpha(q)$ is obtained with the following formula [2]:

$$\alpha(q) = \frac{\partial \tau(q)}{\partial q} \tag{12}$$

All singularity indices $\alpha(q)$ are diffusely distributed, thus constituting a continuous spectrum of $f(\alpha)$ (Figure 7d) [2,70]:

$$f(\alpha(q)) = q\alpha(q) - \tau(q), \tag{13}$$

where $\alpha(q)$ indicates how the fractal ensemble is distributed at various scales and $f(\alpha)$ is a function that represents the distribution of fractal dimensions. The fractal dimensions at different scales can be characterized by the multifractal spectrum curve, which presents a bell-shaped unimodal curve if the geometry is multifractal.

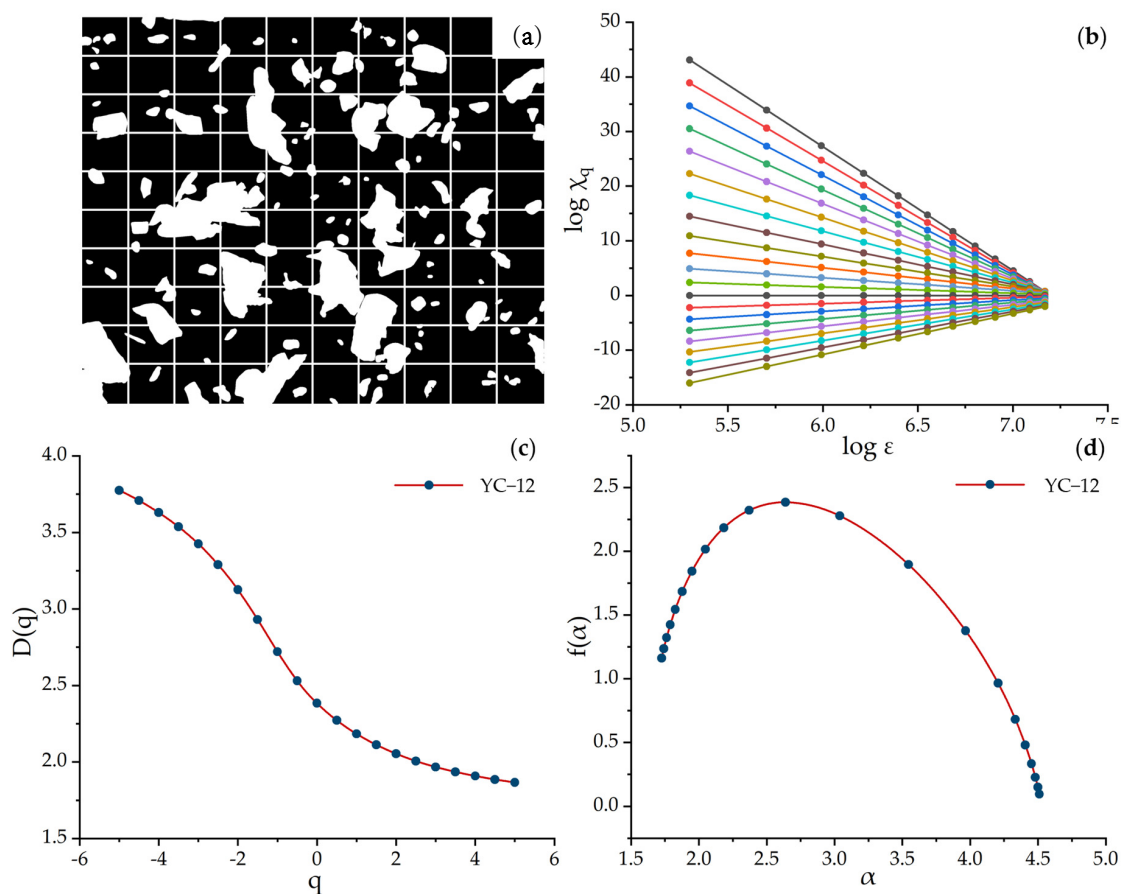


Figure 7. Multifractal calculation of target mineral grains. (a) Subdivision of annotated image by a number of boxes with a size of ϵ pixels. (b) The partition function (χ_q) obtained for different box sizes (ϵ). (c) Generalized fractal dimension (D_q) spectrum. (d) Multifractal fractal spectrum curve of $f(\alpha)$ consisting of diffusely distributed singularity indices ($\alpha(q)$).

The spectral width, $\Delta\alpha$, of the multifractal spectrum quantifies the range of singularity strength, i.e., the magnitude of the probability distribution, which is described as [74]

$$\Delta\alpha = \alpha_{max} - \alpha_{min}, \quad (14)$$

where α_{max} and α_{min} are the maximum value and minimum value, respectively, of the singularity strength. The low-probability subset is reflected by α_{max} , whereas the high-probability subset is reflected by α_{min} . The pseudo code of the moment method for multifractal analysis is listed in Algorithm 2. In addition, we provide an open-source repository designed to facilitate the application of fractal-based pattern quantification of mineral grains, including box-counting calculation, P-A fractal modeling, multifractal analysis. The source code can be found at <https://github.com/YueLiuxx/Python-for-Fractal-based-Pattern-Quantification-of-Mineral-Grains> (accessible on 15 December 2023) and enables researchers to easily implement the fractal-based framework of mineral characterization proposed in this study.

Algorithm 2: The moment method for multifractal analysis**Input:** Image dataset I , list of q values Q , list of box sizes B .**Output:** The generalized fractal dimension D_q ; the singularity index α , multifractal spectrum F .

```

for image in  $I$  do
  for  $q$  in  $Q$  do
    for box size in  $B$  do
       $P \leftarrow \text{pixels}(\text{box size})/\text{total\_pixels}(\text{image})$ 
    end
    probabilities.append( $P$ )
    moment  $\leftarrow$  (probabilities,  $q$ )
    fractal_dimension = ( $B$ , moment,  $q$ )
    alpha  $\leftarrow$  ( $q$ , fractal_dimension)
    spectrum  $\leftarrow$  ( $Q$ ,  $I$ , alpha)
  end
   $D_q$ .append(fractal_dimension)
   $\alpha$ .append(alpha)
   $F$ .append(spectrum)
end

```

4. Results and Discussion

4.1. Annotation Effectiveness and Scaling Invariance of Digitized Mineral Grains

The effectiveness of mineral annotation is a prerequisite for fractal analysis and thus must be assessed. Three different annotating methods are taken into account in this study, namely, manual annotation, direct image binarization and automatic annotation. All three methods are implemented on both the scanned images of polished hand specimens and the photomicrographs of thin sections (Figures 8 and 9).

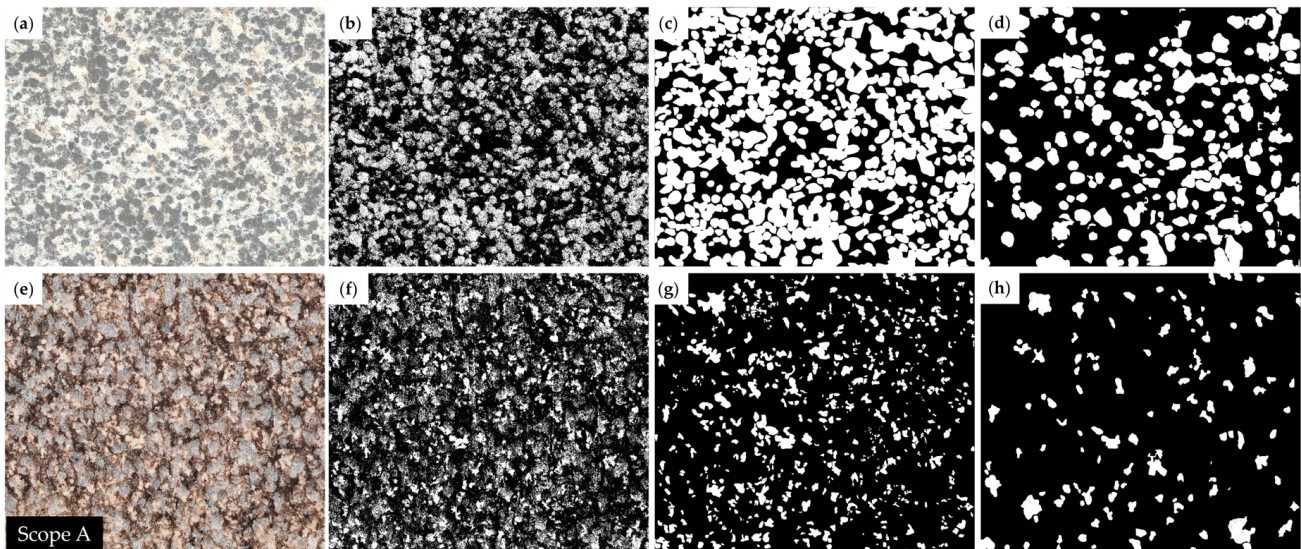


Figure 8. Annotated results of scanned images of polished specimens. (a) Original quartz-bearing image. (b) Direct binarization of quartz grains. (c) Manual annotation of quartz grains. (d) Automatic annotation of quartz grains. (e) Original albite-bearing image. (f) Direct binarization of albite grains. (g) Manual annotation of albite grains. (h) Automatic annotation of albite grains.

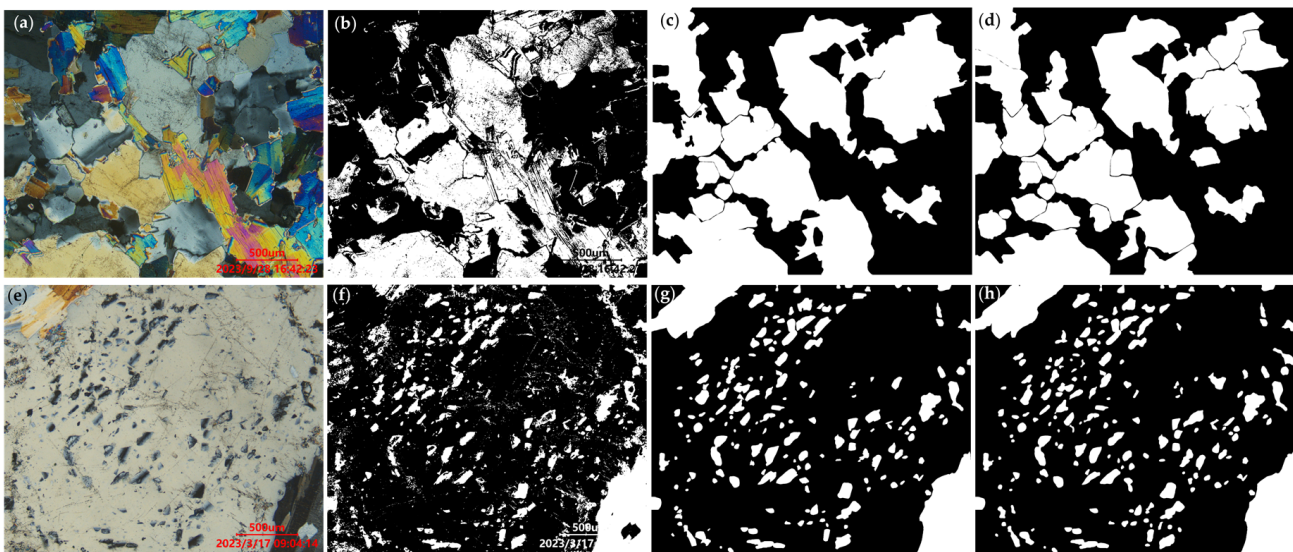


Figure 9. Annotated results of photomicrographs of thin sections. (a) Original quartz-bearing image; (b) Direct binarization of quartz grains. (c) Manual annotation of quartz grains. (d) Automatic annotation of quartz grains. (e) Original albite-bearing image. (f) Direct binarization of albite grains. (g) Manual annotation of albite grains. (h) Automatic annotation of albite grains.

Manual annotation of target minerals is quite time-consuming but the most accurate. We serve the results of manual annotation as benchmark patterns. Direct binarization implemented based on RGB color thresholds and automatic annotation conducted with the aid of the SAM are compared with the template of manual annotation. As shown in Table 1, the annotated results of direct binarization exhibit relatively stable accuracy of D_b , with errors ranging from 0.88% to 1.62%, regarding different target minerals in both specimens and thin sections. Such errors are attributed to the similarity in the gray distribution of a portion of quartz and albites (Figures 8b,f and 9b,f), especially in some thin sections where the color contrast between these two minerals is extremely subtle (e.g., upper-left corner of Figure 9e). Therefore, this approach is considered valid only when the mineral grains can be clearly distinguished by natural color. In contrast, the results of automatic annotation show a remarkable accuracy difference between specimens (5.71% error for quartz and 6.90% error for albite) and thin sections (0.58% error for quartz and 0.61% error for albite). On the one hand, automatic annotation also suffers from low color contrast among adjacent mineral grains (Figure 8d,h), leading to poor performance in mineral annotation for scanned images of specimens. On the other hand, benefiting from the employment of the crossed-polarized light of a microscope, each target mineral in thin sections shows an exclusive interference color, which results in a precise annotated result of mineral grains in photomicrographs.

Table 1. Evaluation results of different digitization methods.

Type	Manual Annotation		Direct Binarization		Automatic Annotation	
	D_b	D_b	D_b	Error of D_b	D_b	Error of D_b
Quartz in hand specimen	1.8584	1.8885	1.8885	1.62%	1.7522	5.71%
Albite in hand specimen	1.6439	1.8755	1.8755	1.41%	1.5305	6.90%
Quartz in thin section	1.8616	1.8452	1.8452	0.88%	1.8508	0.58%
Albite in thin section	1.6889	1.7335	1.7335	2.64%	1.6786	0.61%

D_b : box-counting dimension.

The fractality of the target mineral in YCRMG was evaluated using three different scales of hand specimens and thin sections (Figure 10), namely, a thin-section scale of 1.04~1270.5 μm under tenfold (10 \times) magnification, a thin-section scale of 2.10~2571.43 μm under fivefold (5 \times) magnification and a hand-specimen scale of 21.37~52,300 μm . As

depicted in Figure 10, $N(r)$ and r show a great power-law relationship at all three scales, with coefficients of determination (R^2) greater than 0.995. The fractal dimensions are obtained from the slopes of the fitting lines, which are 1.6618, 1.6786 and 1.6439, respectively. It can be concluded that mineral grains derived from YCRMG exhibit strong scale invariance within the range of 1.04 to 52,300 μm and that the fractal dimensions calculated at three scales are numerically similar.

Based on the above assessment of both method effectiveness and scale variation, it can be inferred that automatic annotation aided by the SAM is favorable for processing a large number of photomicrographs in thin sections due to its high efficiency and perfect accuracy (Table 1). In addition, the fractal dimension calculated through automatic annotation at the thin-section scale can well represent the fractality in the whole observed microscopic range (Figure 10b). In this regard, automatic annotation is deemed the optimal method in this study to extract microscopic morphological information of mineral grains utilized for fractal analyses.

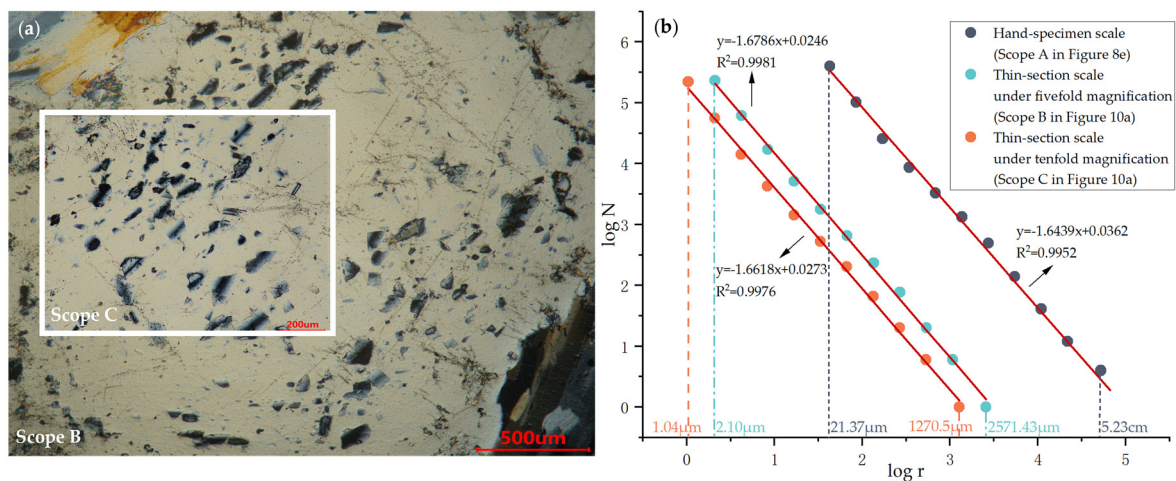


Figure 10. (a) Photomicrographs showing target albites under fivefold magnification (Scope B) and tenfold magnification (Scope C). (b) Fractal calculation at three different scales within a range of 1.04 μm ~52,300 μm .

It is noteworthy that the SAM-based automatic annotation employed in this study is an initial exploration of the SAM in mineralogical research. The results of our study demonstrate its distinguishing advantages when tackling photomicrographs of mineral grains. Essentially, the SAM offers zero-shot generation for irregular mineral geometries without any additional training. This capability is of great significance for segmenting and identifying diverse minerals, which often exhibit various colors, phases, crystal shapes and textures. In this regard, the SAM holds a promising future perspective in image-related mineralogical research. For instance, the SAM can be used in image segmentation and object detection in remote sensing data, assisting in mapping hydrothermally altered minerals on a regional scale. The feasibility of this application is supported by a recently published study which employs the SAM to effectively map land cover based on remote sensing data [75]. In addition, the framework of SAM-based automatic annotation can be readily applied to segment scanning electron microscopy (SEM) images, which would greatly boost the micrometer-dimensioned characterization of mineral identity, morphology, microstructure and petrological context, which is currently based on manual segmentation [31,76]. To sum up, the SAM exhibits favorable potential to benefit mineral-related image processing in a wide range spanning from kilometer-level mapping to micron-scale annotation.

4.2. Fractal Results of Regular Minerals

The mineral grains of quartz, lepidolite and albite were automatically annotated from the original photomicrographs (Figure 11), based on which a series of fractal dimensions were calculated, and the results are listed in Table 2.

The results of the box-counting analysis indicate a strong power-law relationship between the number of boxes (N) and box size (r) with high coefficients of determination (R^2), greater than 0.98 (Figure 12). The resulting D_b denotes the inhomogeneity of the mineral grain distribution [30], which reveals that quartz (average $D_b = 1.8254$) is more inhomogeneous than lepidolite (average $D_b = 1.7903$) and albite (average $D_b = 1.6811$). D_{PA} , commonly serving as an exponent indicative of the irregularity degree in the boundaries of different grains [19], was obtained from Figure 13, which shows a good scaling invariance of perimeter versus area. Quartz yields the greatest average D_{PA} value of 1.3288, followed by lepidolite (1.2299) and albite (1.1402), which is consistent with the order of D_b values.

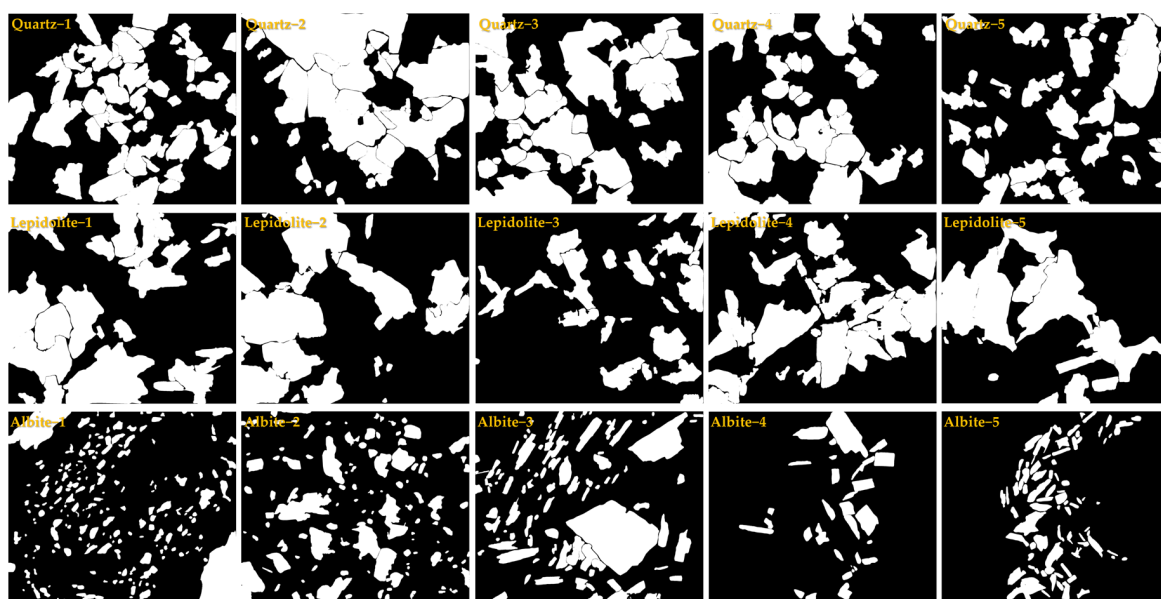


Figure 11. Annotation of typical minerals from original photomicrographs (exhibited in Figure 3).

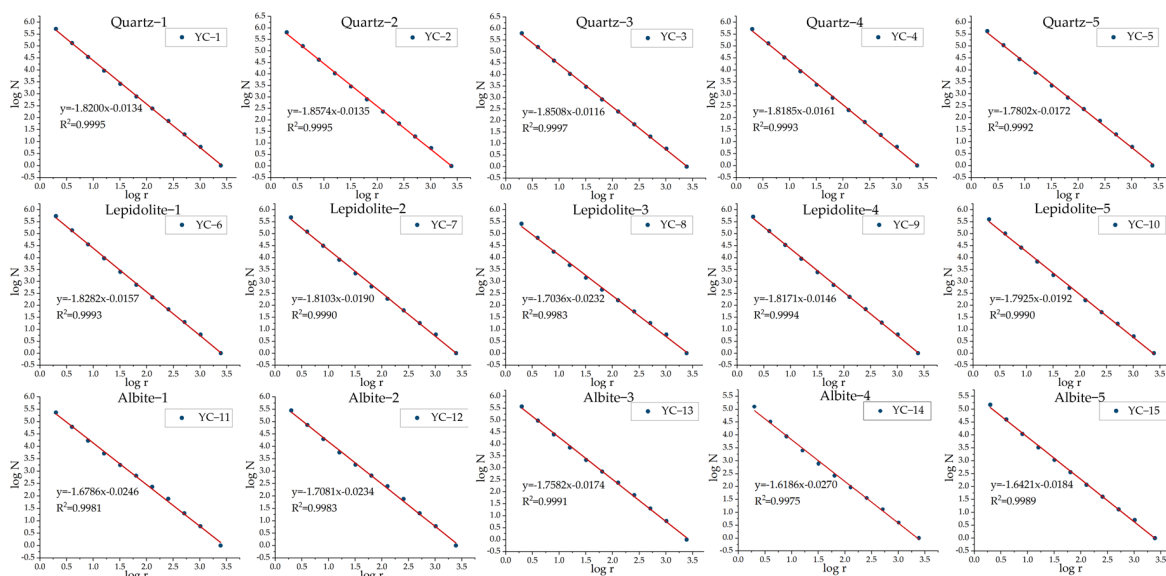


Figure 12. Results of the box-counting fractal analyses conducted in the log–log graph of box number ($N(r)$) versus box size (r).

Table 2. Results of fractal parameters for different types of mineral grains.

Type	Sample ID	D_b	D_{PA}	$\Delta\alpha$	$\Delta f(\alpha)$	D_1	D_2	
Quartz	YC-1	1.8200	1.4669	3.6286	−1.8697	2.2145	2.1590	
	YC-2	1.8574	1.2687	4.0856	−1.9460	2.1887	2.1429	
	YC-3	1.8508	1.3864	3.8167	−1.8730	2.2424	2.1868	
	YC-4	1.8185	1.3047	4.3445	−1.8898	2.1370	2.0755	
	YC-5	1.7802	1.2175	3.0268	−1.5048	2.2179	2.1514	
	Average	1.8254	1.3288	3.7804	−1.8167	2.2001	2.1431	
Lepidolite	YC-6	1.8282	1.2519	4.9942	−2.0312	2.1434	2.0944	
	YC-7	1.8103	1.2279	2.7845	−1.6092	2.0748	2.0339	
	YC-8	1.7036	1.1859	4.5831	−1.4189	1.9764	1.8883	
	YC-9	1.8171	1.2250	3.9381	−1.8866	2.1777	2.1198	
	YC-10	1.7925	1.2588	4.1050	−1.8987	1.9925	1.9438	
	Average	1.7903	1.2299	4.0810	−1.7689	2.0730	2.0160	
Regular albite	YC-11	1.6786	1.1272	3.9592	−0.6902	2.1336	1.9467	
	YC-12	1.7081	1.1420	2.7851	−1.0666	2.1837	2.0538	
	YC-13	1.7582	1.1525	2.6094	−1.2967	2.1727	2.0609	
	YC-14	1.6186	1.0885	3.1784	−0.5825	1.8114	1.7302	
	YC-15	1.6421	1.1908	4.7901	−1.3589	1.8019	1.7415	
	Average	1.6811	1.1402	3.4644	−0.9990	2.0207	1.9066	
Semi-snowball-textured albite	YC-26	1.5010	1.1056	3.0812	−0.7106	1.5031	1.4325	
	YC-27	1.4350	1.1514	3.9009	−0.7469	1.6429	1.4895	
	Average	1.4680	1.1285	3.4910	−0.7288	1.5730	1.4610	
	Albite	YC-16	1.6435	1.1772	2.7874	−0.8400	2.1933	2.0679
		YC-17	1.6210	1.2128	3.6872	−1.5564	2.1624	2.0762
		YC-18	1.6648	1.1684	3.5903	−0.6507	2.2799	2.1949
Snowball-textured albite		YC-19	1.5735	1.2008	3.0605	−1.3445	2.2126	2.1110
		YC-20	1.5700	1.2208	2.9349	−1.3785	2.2424	2.1424
		YC-21	1.6491	1.2582	3.4213	−1.0524	2.1445	2.0488
		YC-22	1.6269	1.1812	2.2822	−0.9818	2.2500	2.1664
YC-23		1.6328	1.2071	3.3678	−0.9127	2.2508	2.1638	
Average	1.6227	1.2033	3.1415	−1.0896	2.2170	2.1214		
Outer albite crystal	YC-21	1.7305	1.2789	3.1526	−1.3348	1.8325	1.7693	
	YC-25	1.7186	1.2486	2.7577	−1.4705	1.8181	1.7745	
	YC-27	1.7772	1.2159	3.9384	−1.3343	1.9612	1.8913	
	Average	1.7421	1.2478	3.2829	−1.3799	1.8706	1.8117	

D_b : box-counting dimension; D_{PA} : perimeter–area fractal dimension; $\Delta\alpha$: spectral width of the multifractal spectrum; $\Delta f(\alpha)$: difference between $f(\alpha_{min})$ and $f(\alpha_{max})$; D_1 : information dimension; D_2 : correlation dimension.

The spectra of the generalized fractal dimension (D_q) are illustrated in Figure 14. D_q is negatively correlated with q , exhibiting an inverse S shape, which behaves as a typical multifractal pattern [74]. D_1 and D_2 , reflecting the degree of self-similarity of grain distribution, were acquired from the D_q spectra [77], and indicate that quartz exhibits better self-similarity than the other two minerals, according to the descending order of D_1 and D_2 values for quartz, lepidolite and albite (Table 2).

Figure 15 displays the relationship between $f(\alpha)$ and $\alpha(q)$, which shows a typical bell shape. The width of the multifractal spectrum ($\Delta\alpha$ ($\Delta\alpha = \alpha_{max} - \alpha_{min}$)) indicates the heterogeneity of the probability distribution in the target fractal structure [78]. In this regard, lepidolite, with the greatest value of 4.0810, is more heterogeneous in the probability distribution than quartz (3.7804) and albite (3.4644). $\Delta f(\alpha)$, which is calculated as $f(\alpha_{min}) - f(\alpha_{max})$, reflects the asymmetry of the multifractal singularity spectrum [78]. If $\Delta f(\alpha) > 0$, it implies that the low-probability subset dominates the whole fractal set, and vice versa. The values of $\Delta f(\alpha)$ in this study are all negative, indicating that a high-probability subset, i.e., fine grains in this study, dominates the fractal set of mineral grains.

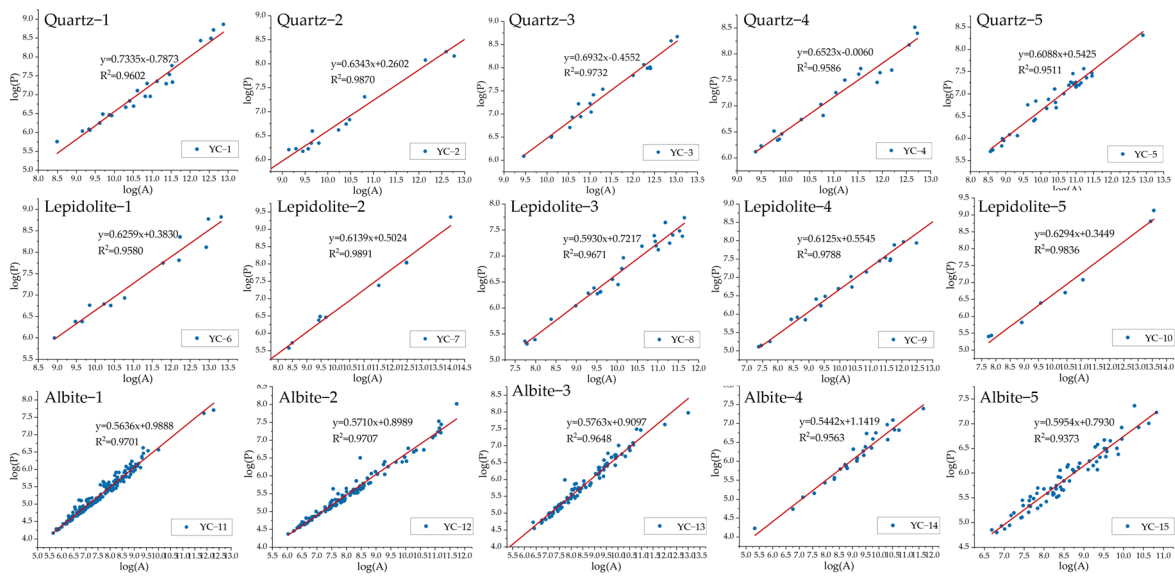


Figure 13. Results of the perimeter-area fractal analyses conducted in the log-log graph of perimeter (P) versus area (A).

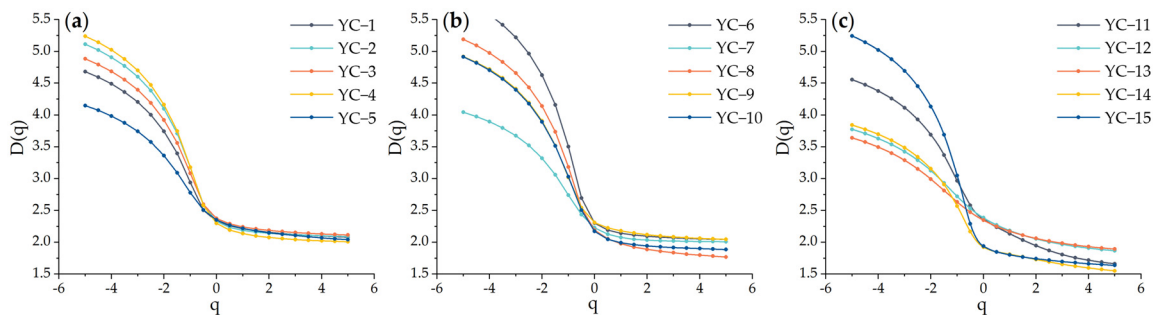


Figure 14. Generalized fractal dimension spectra of quartz (a), lepidolite (b) and albite grains (c).

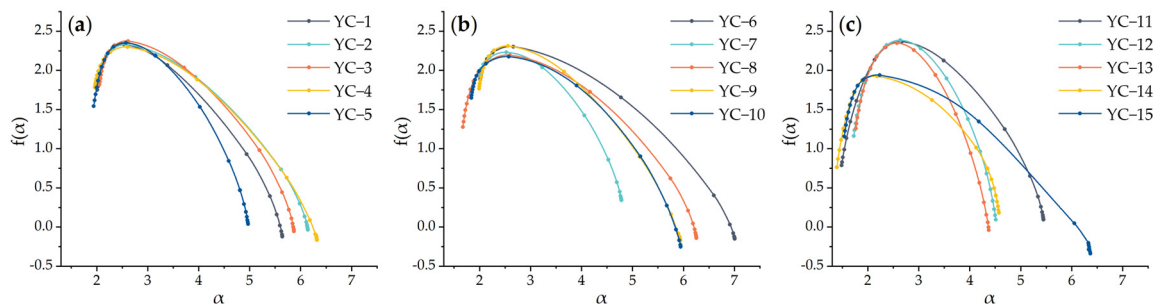


Figure 15. Multifractal spectra of quartz (a), lepidolite (b) and albite grains (c).

All the fractal dimensions mentioned above can be used to depict different aspects of mineral irregularity. Various combinations of these fractal dimensions were tested to seek the best indicator for distinguishing the target minerals. The results indicate that D_b and D_{PA} outperform other combinations of fractal indices in revealing the intrinsic morphological features of quartz, lepidolite and albite. Two linear boundaries well distinguishing the three target minerals can be drawn in a diagram with the x-axis of D_{PA} versus the y-axis of D_b (Figure 16). Within this scenario, quartz points are plotted near the upper-right corner, whereas albite points are located in the bottom-left corner. Lepidolite points are sandwiched between the former two mineral points (Figure 16). Such distinct distribution patterns suggest that a specific mineral can be distinguished from other minerals with the assistance of quantitative fractal indices. This implication would benefit mineral identification, which

plays a fundamental role in mineralogical research. Mineral identification has been boosted by AI-driven intelligent classification in recent years [79–81]; however, its capability is subject to the limited selection of features, which are mostly optical characteristics derived from thin sections. An introduction of the proposed SAM-based framework and its resulting fractal characterization can enhance the performance of intelligent mineral recognition. First, image segmentation is a prerequisite step of mineral identification, which can be significantly improved by employing the SAM, as mentioned above. Second, fractal dimensions reflect inherent features of mineral morphology, which can be served as strong input feature layers that enhance the generalization capability of machine learning-based classification model. At last, the fractal dimensions provide a quantitative measurement of target minerals, which can be readily integrated into the training dataset without any data processing, thus avoiding the mixture of noise data that plausibly produced by data processing.

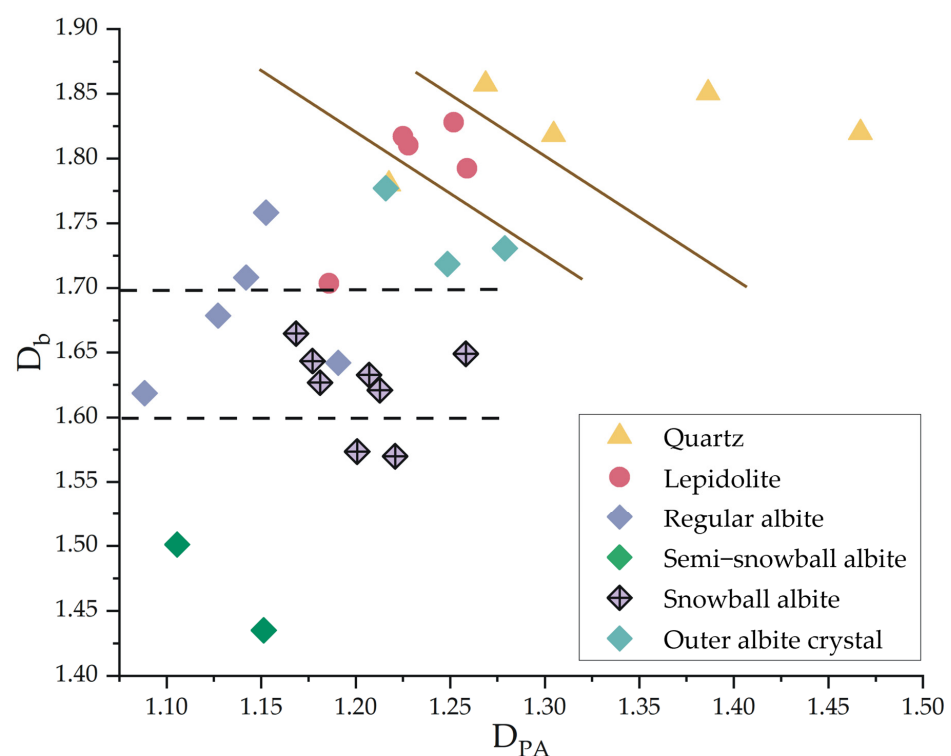


Figure 16. $D_{PA}-D_b$ schematic diagram for distinguishing target minerals and textures.

It should be noted that the fractal pattern varies according to the minerals derived from different ore deposits, which are products of diverse ore-forming mechanisms. For example, the distributions of quartz aggregates in granites derived from the Severyn pluton, Central Kazakhstan and Aetyka pluton are characterized by D_b values, which vary mostly from 1.75 to 1.81 for standard granites, from 1.63 to 1.70 for alaskite granites and from 1.48 to 1.62 for amazonite granites [82]. According to quartz samples from five types of mylonites within the foreland of the Moine Thrust Zone in NW Scotland, the values of D_{PA} vary from 1.20 to 1.60 with the increase in the degree of deformation [28]. It implies that the morphological fractal indices attached to a specific formative environment can be used to trace nonlinear behaviors in the process of mineral formation. In order to further reveal such pattern-forming processes, the snowball texture, which is well recognized as a striking symbol of highly evolved granites [42,43], is investigated in detail.

4.3. Fractal Results of Snowball Texture and Their Implication for Mineral Growth Mechanism

The snowball texture is ubiquitous in YCRMG. Snowball-textured albites have featured fractal dimensions that differ from those of other albites (Figure 16 and Table 2). Compared

with regular albites, the albite laths in the snowball texture have greater values of D_{PA} and lower values of D_b (Figure 16). Among the snowball albites, some unmaturing banding textures are discernible, which can be referred to as “semi-snowball” textures (Figure 16). The analytical results indicate that the D_b values of albites in the semi-snowball texture are much lower than those in the snowball texture. The above results imply that the morphological fractal indices can be employed not only to distinguish the special mineral texture from the regular form but also to quantitatively measure the maturity of the special texture, which implies that the fractal dimensions may be closely related to the growth processes of minerals.

Many previous studies have demonstrated that the growth of minerals is a fractal process that results in a characteristic fractal dimension [83–86]. For example, the Diffusion Limited Aggregation (DLA) model, proposed by Witten and Sander [85], has been employed to simulate the process of mineral crystal growth [84]. The DLA model suggests that the d -dimensional aggregates grow upon a single-seed particle, showing a fractal relationship in which the total number of particles (N) scales with the linear dimension (R) as $N \propto R^{D(d)}$, where $D(d)$ is the fractal dimension [86]. Theoretically, $D(d)$ is a universal quantity given approximately by $D(b) \approx \frac{5}{6}d$. As our study implemented in two-dimensional images, $D(d)$ is approximate to 1.67 [86]. This value may vary within a range of 1.6–1.7 in practical calculations. It is interesting to note that the D_b values of most snowball-textured albites fall within the range between 1.6 and 1.7, where no lepidolite nor quartz occur (Figure 16). Such result coincides with the fractal dimension yielded by the DLA model. Although no modeling works have been conducted in the study area to simulate the mineral growth processes, the clustered pattern together with the coincidence of identical fractal dimensions imply that the snowball-textured albites grow in a kinetic manner which differs from that of regular albites and other minerals in YCRMG.

In order to trace the footprints of the pattern-forming process, the banding of snowball was divided into inner, middle and outer zones, based on which the fractal and multifractal dimensions were calculated (Figure 17 and Table 3). The results indicate that the values of all the fractal indices, including D_b , D_1 , D_2 , $\Delta\alpha$ and $\Delta f(\alpha)$, strictly increase from core to rim, forming a “fractal-index banding” in the radar diagram (Figure 17d). This finding implies that the complexity of banded albite decreases from the outer spaces to the core zones. In addition, it is commonly observed in YCRMG that the snowball quartz is commonly enclosed by large albite crystals (Figures 2d and 17c). The fractal indices of these albites were also calculated and are plotted in Figure 17d. The outer large albites have greater values of fractal indices than the three zones of the snowball texture, with the exception of the value of $\Delta\alpha$, which is smaller than that of the outer zones of the snowball texture.

The so-called “snowball quartz” is a common feature of rare-metal granites and is considered an important indicator of the origin of its host rocks, but the origin of the typical texture itself remains controversial [44,87–91]. As far as the “snowball quartz” in YCRMG is concerned, Pollard adopted the currently popular magmatic perspective [43], i.e., snowball-textured albite laths were simultaneously formed and then were included and arranged along the growth zones by some more rapidly crystallized quartz phenocrysts, while Wu et al. attributed it to metasomatic processes but suggested that snowball quartz replaced the enclosed “tabular albite” [44]. Based on these two models, the albite grains inside and outside the snowball quartz simultaneously formed, and both should have identical morphological complexity, which is contrary to the results of this study. In contrast, a two-phase model was proposed to explain the origin of the snowball texture from a metasomatic perspective [92]. In the early phase, quartz metacrysts were formed through self-purification, which squeezed out some alkaline inclusions confined to the hexagon-zoned crystallographic orientations. In the second phase, the responsible fluids supposedly flowed into the pre-existing metacrysts from rim to core through microfractures and gradually reacted with and altered the zoned alkaline composition, leading to the formation of albites that exhibit a zonal distribution identical to that of the pre-existing hexagon-shaped oriented inclusions. In this interpretation, the degrees of morphological

complexity and textural maturities among different zones of the snowball texture are uneven. The outer zones have experienced more plentiful fluids and longer durations of alteration and thus have greater fractal indices, which represent higher complexity of evolved texture, which explains the variation law of fractal dimensions from rim to core. Therefore, the results of our study support the two-phase metasomatic origin of the snowball texture. In fact, evidence of hydrothermal fluid activity has been widely identified in rare-metal granites [91], and the fluid role in rare-metal mineralization has been highlighted by many scholars [44,91], regardless of their basic magmatic or metasomatic points of view. This recognition enables our explanation model linking fractal characteristics with fluid activity to be more compatible with future updated models.

Our findings prove that fractal-index quantification provides valuable references for tracing and understanding the formation process of the snowball texture. This application can be extended to broader fields of granite-related mineralogical research. The origin of granite has been discussed for dozens of years and is considered a puzzling topic in geology, and the investigation of mineral texture is exactly one of the keys to this significant issue. In addition to the snowball texture, other mineral textures of granite, such as myrmekitic texture, perthitic texture and graphic texture, have also attracted great attention due to their implications for revealing mechanisms of diagenesis and/or metamorphism [93]. The fractal characterization resulted from the proposed framework contributes to interpreting evolving behaviors of the complex textures in a quantitative manner, which would enrich the thoughts of mineralogical study and facilitate the research progress on granite genesis.

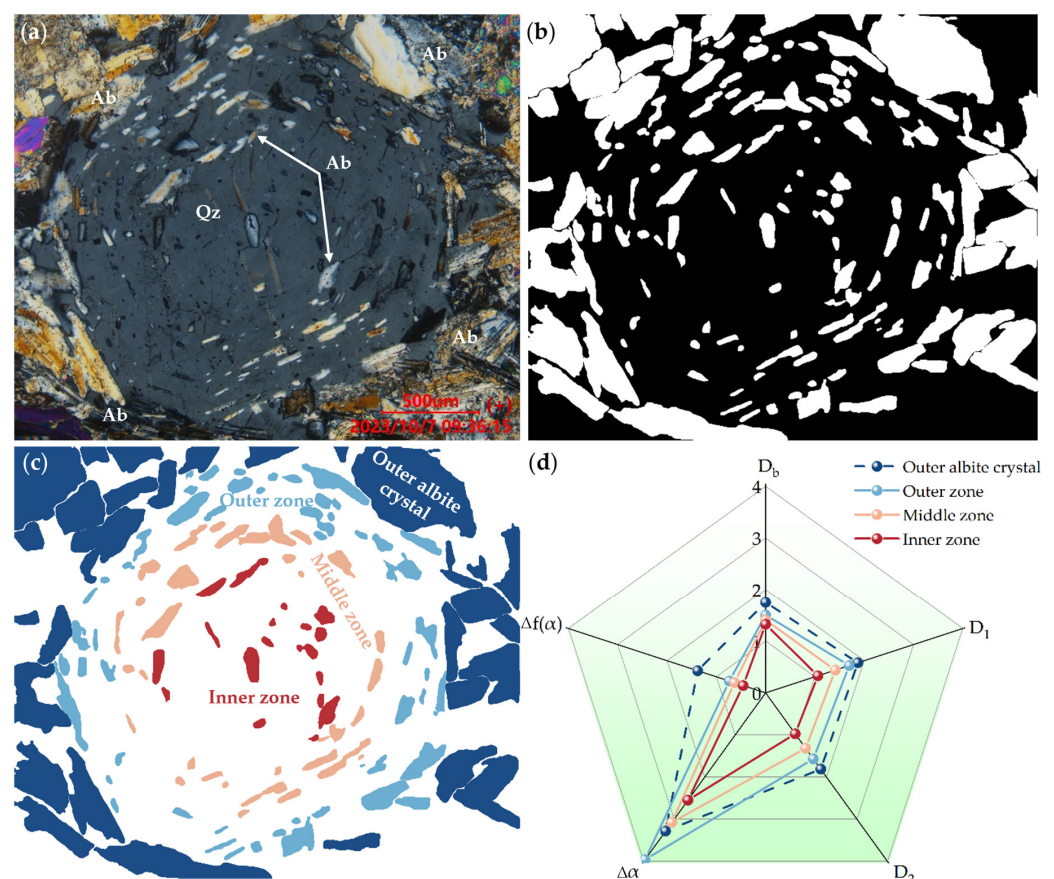


Figure 17. (a) Original photomicrograph of the snowball texture. (b) Annotated image of snowball-textured albites. (c) Zoning of snowball-textured albites. (d) Radar diagram of resultant fractal dimensions of different albite zones.

Table 3. Results of fractal analyses on albites in different zones of snowball texture.

Zoning	Sample ID	D_b	$\Delta\alpha$	$\Delta f(\alpha)$	D_1	D_2
Inner zone	YC-21	1.3168	2.0766	−0.5948	1.1512	1.0712
	YC-22	1.3259	3.2804	−0.4891	1.2138	1.1212
	YC-23	1.4291	2.7697	−0.8997	1.3692	1.2596
	YC-24	1.3202	1.5866	−0.2938	0.9795	0.8920
	YC-25	1.3601	3.3444	−0.2003	1.2696	1.1309
	YC-26	1.2109	1.6502	−0.3798	0.7395	0.7140
	YC-27	1.2721	3.1262	−0.3271	0.7104	0.6259
	Average	1.3193	2.5477	−0.4549	1.0619	0.9736
Middle zone	YC-21	1.4161	3.2073	−0.7647	1.4904	1.3914
	YC-22	1.4417	3.3638	−1.0268	1.6271	1.5178
	YC-23	1.4138	3.1278	−0.8177	1.6782	1.5823
	YC-24	1.4799	2.7211	−0.4022	1.4465	1.3136
	YC-25	1.4252	2.9262	−0.4841	1.5103	1.4107
	YC-26	1.3576	2.4595	−0.5084	1.0671	1.0271
	YC-27	1.2612	3.7482	−0.4169	1.0755	0.9600
	Average	1.3994	3.0791	−0.6316	1.4136	1.3147
Outer zone	YC-21	1.5966	4.0408	−0.9953	1.8990	1.7912
	YC-22	1.5581	2.9119	−0.6970	1.9871	1.8856
	YC-23	1.5521	3.9871	−0.9293	1.9166	1.8190
	YC-24	1.5405	4.8781	−0.4483	1.6594	1.4951
	YC-25	1.5045	4.1987	−1.1991	1.7692	1.6764
	YC-26	1.3969	4.3164	−0.9015	1.3166	1.2190
	YC-27	1.3304	3.3981	0.0256	1.3237	1.0867
	Average	1.4970	3.9616	−0.7350	1.6959	1.5676
Outer albite crystal	YC-21	1.7305	3.1526	−1.3348	1.8325	1.7693
	YC-25	1.7186	2.7577	−1.4705	1.8181	1.7745
	YC-27	1.7772	3.9384	−1.3343	1.9612	1.8913
	Average	1.7421	3.2829	−1.3799	1.8706	1.8117

* D_b : box-counting dimension; $\Delta\alpha$: spectral width of the multifractal spectrum; $\Delta f(\alpha)$: difference between $f(\alpha_{min})$ and $f(\alpha_{max})$; D_1 : information dimension; D_2 : correlation dimension.

5. Conclusions

Fractal-based recognition and quantification of mineral grains are significant for characterizing morphological properties and distribution patterns. However, this task is challenging due to the time-consuming manual annotation of minerals, which is a prerequisite for fractal calculation. In this study, a large model is introduced to build a framework for the automatic annotation of mineral grains. The results demonstrate its feasibility in photomicrograph processing due to (1) the subtle D_b error of only 0.6% compared with manual annotation and (2) scaling invariance at the micro-scale ranging from 1.04 to 52,300 μm , which allows for good representativeness of D_b calculated from automatic annotation.

A series of fractal and multifractal analyses were conducted based on the proposed automatic framework. The resulting indices depict different perspectives of fractal irregularities of target mineral grains. D_b and D_{PA} , which serve as indicators of the inhomogeneity of mineral grain distribution and the irregularity degree of grain boundaries, exhibit the descending order of quartz > lepidolite > albite. D_1 and D_2 also yield identical patterns, reflecting that quartz has better self-similarity of grain distribution than lepidolite and albite. The multifractal spectrum indicates that lepidolite is more heterogeneous in the probability distribution than quartz and albite. In addition, fine grains dominate the fractal set of mineral grains according to the negative values of $\Delta f(\alpha)$. The three studied minerals can be well distinguished by their intrinsic morphological characteristics in a $D_{PA}-D_b$ diagram, in which lepidolites are sandwiched between upper-right quartz and bottom-left albites.

The snowball texture, which is recognized as a striking symbol of highly evolved granites, was investigated in detail to reveal pattern-forming processes. Snowball-textured

albites exhibit characteristic D_b values ranging from 1.6 to 1.7, which differ from regular albites and coincide with fractal indices derived from the fractal growth model. The fractal indices, including D_b , D_1 , D_2 , $\Delta\alpha$ and $\Delta f(\alpha)$, strictly decrease from rim to core, suggesting that the outer zones have higher complexity and maturity of the evolving system. This finding may be attributed to a gradual evolving process related to the responsible fluids flowing from rim to core, resulting in the formation of zonal albites with different morphological irregularities, which supports a metasomatic origin of snowball texture.

The findings of this study demonstrate the effectiveness and efficiency of the proposed framework in characterizing mineral morphology and distribution patterns. Future attempts can be made to broaden its applications in image-related mineralogical research ranging from regional-scale mineral mapping to micron-scale mineral annotation. The resulting fractal indices reflect the inherent morphological features of mineral grains and thus can be readily integrated into intelligent systems for mineral identification, enhancing the generalization capability of AI-driven classification models. Future efforts can also be made to deepen the findings of this study by transferring the framework to other complex mineral textures in the granites, so as to facilitate the understanding of rock-forming and ore-forming processes. Furthermore, we provide the open-access code designed to implement the proposed framework on an online repository, encouraging further and broader applications of SAM-based segmentation and fractal-index quantification in the geological domain.

Author Contributions: Conceptualization, T.S. and K.W.; methodology, Y.L. and T.S.; software, Y.L. and M.F.; validation, Y.L., T.S. and K.W.; formal analysis, H.Z. and J.Z.; investigation, Y.L., X.J. and Q.L.; resources, K.W.; writing—original draft preparation, Y.L. and T.S.; writing—review and editing, Y.L., T.S. and K.W.; visualization, Y.L.; project administration, T.S. and K.W.; funding acquisition, T.S. and K.W. All authors have read and agreed to the published version of the manuscript.

Funding: This research was funded by National Natural Science Foundation of China (grant Nos. 42062021 and 41963005); Natural Science Foundation of Jiangxi Province for Distinguished Young Scholars (grant No. 20224ACB218003); China Postdoctoral Science Foundation (grant No. 2019M662267); Natural Science Foundation of Jiangxi Province (grant No. 20202BAB203016); Program of Qingjiang Excellent Young Talents, Jiangxi University of Science and Technology (grant No. JXUSTQJBJ2020001); Science and Technology Program of Ganzhou City (grant No. 202101095156); and Postgraduate Innovation Program of Jiangxi Province (grant No. YC2024-S682).

Data Availability Statement: Data are contained within the article.

Acknowledgments: We are grateful to two anonymous reviewers for their constructive comments, which significantly improved the manuscript.

Conflicts of Interest: The authors declare no conflicts of interest.

References

1. Mandelbrot, B.B. The Fractal Geometry of Nature. *Am. J. Phys.* **1983**, *51*, 286–287. [[CrossRef](#)]
2. Evertsz, C.J.; Mandelbrot, B.B. Multifractal measures. *Chaos Fract.* **1992**, *1992*, 921–953.
3. Wilson, B.; Dewers, T.; Reches, Z.; Brune, J. Particle size and energetics of gouge from earthquake rupture zones. *Nature* **2005**, *434*, 749–752. [[CrossRef](#)]
4. Lopes, R.; Betrouni, N. Fractal and multifractal analysis: A review. *Med. Image Anal.* **2009**, *13*, 634–649. [[CrossRef](#)] [[PubMed](#)]
5. Zhu, P.; Cheng, Q.; Chen, G. New fractal evidence of Pacific plate subduction in the late Mesozoic, Great Xing'an range, Northeast China. *J. Earth Sci-China* **2019**, *30*, 1031–1040. [[CrossRef](#)]
6. Cheng, Q. Fractal Derivatives and Singularity Analysis of Frequency—Depth Clusters of Earthquakes along Converging Plate Boundaries. *Fractal Fract.* **2023**, *7*, 721. [[CrossRef](#)]
7. Ali, S.M.; Abdelrahman, K. The Impact of Fractal Dimension, Stress Tensors, and Earthquake Probabilities on Seismotectonic Characterisation in the Red Sea. *Fractal Fract.* **2023**, *7*, 658. [[CrossRef](#)]
8. Zhu, P.; Liu, Y.; Cheng, Q. The spatial distribution differences between Jiaodong and Luxi terrane gold deposits by fractal method and its implications for the source of gold. *Miner. Depos.* **2023**, *42*, 639–645. (In Chinese with English abstract)
9. Agerberg, F.P. Fractals and spatial statistics of point patterns. *J. Earth Sci.-China* **2013**, *24*, 1–11. [[CrossRef](#)]
10. Chen, G.; Liu, T.; Sun, J.; Cheng, Q.; Sahoo, B.; Zhang, Z.; Zhang, H. Gravity method for investigating the geological structures associated with W–Sn polymetallic deposits in the Nanling Range, China. *J. Appl. Geophys.* **2015**, *120*, 14–25. [[CrossRef](#)]

11. Sun, T.; Chen, F.; Zhong, L.; Liu, W.; Wang, Y. GIS-based mineral prospectivity mapping using machine learning methods: A case study from Tongling ore district, eastern China. *Ore Geol. Rev.* **2019**, *109*, 26–49. [CrossRef]
12. Sun, T.; Li, H.; Wu, K.; Chen, F.; Zhu, Z.; Hu, Z. Data-driven predictive modelling of mineral prospectivity using machine learning and deep learning methods: A case study from southern Jiangxi Province, China. *Minerals* **2020**, *10*, 102. [CrossRef]
13. Zuo, R.; Cheng, Q.; Xia, Q.; Agterberg, F. Application of fractal models to distinguish between different mineral phases. *Math. Geosci.* **2009**, *41*, 71–80. [CrossRef]
14. Cai, Q.; Tan, K.; Zhu, J.; Zeng, S. Multifractal Characteristics of Uranium Grade Distribution and Spatial Regularities in a Sandstone-Type Uranium Deposit in Xinjiang, China. *Fractal Fract.* **2023**, *7*, 704. [CrossRef]
15. Xiao, F.; Wang, K.; Hou, W.; Erten, O. Identifying geochemical anomaly through spatially anisotropic singularity mapping: A case study from silver-gold deposit in Pangxidong district, SE China. *J. Geochem. Explor.* **2020**, *210*, 106453. [CrossRef]
16. Xiao, F.; Chen, J.; Hou, W.; Wang, Z.; Zhou, Y.; Erten, O. A spatially weighted singularity mapping method applied to identify epithermal Ag and Pb-Zn polymetallic mineralization associated geochemical anomaly in Northwest Zhejiang, China. *J. Geochem. Explor.* **2018**, *189*, 122–137. [CrossRef]
17. Liu, Y.; Cheng, Q.; Zhou, K. New insights into element distribution patterns in geochemistry: A perspective from fractal density. *Nat. Resour. Res.* **2019**, *28*, 5–29. [CrossRef]
18. Zuo, R.; Carranza, E.J.M.; Cheng, Q. Fractal/multifractal modelling of geochemical exploration data. *J. Geochem. Explor.* **2012**, *122*, 1–3. [CrossRef]
19. Cheng, Q. The perimeter-area fractal model and its application to geology. *Math. Geol.* **1995**, *27*, 69–82. [CrossRef]
20. Zhang, Z.; Mao, H.; Cheng, Q. Fractal geometry of element distribution on mineral surfaces. *Math. Geol.* **2001**, *33*, 217–228.
21. Cheng, Q. Mapping singularities with stream sediment geochemical data for prediction of undiscovered mineral deposits in Gejiu, Yunnan Province, China. *Ore Geol. Rev.* **2007**, *32*, 314–324. [CrossRef]
22. Li, C.; Ma, T.; Shi, J. Application of a fractal method relating concentrations and distances for separation of geochemical anomalies from background. *J. Geochem. Explor.* **2003**, *77*, 167–175. [CrossRef]
23. Afzal, P.; Alghalandis, Y.F.; Khakzad, A.; Moarefvand, P.; Omran, N.R. Delineation of mineralization zones in porphyry Cu deposits by fractal concentration–volume modeling. *J. Geochem. Explor.* **2011**, *108*, 220–232. [CrossRef]
24. Cheng, Q.; Xu, Y.; Grunsky, E. Integrated spatial and spectrum method for geochemical anomaly separation. *Nat. Resour. Res.* **2000**, *9*, 43–52. [CrossRef]
25. Liu, Y.; Zhou, K.; Cheng, Q. A new method for geochemical anomaly separation based on the distribution patterns of singularity indices. *Comput. Geosci.* **2017**, *105*, 139–147. [CrossRef]
26. Xiao, F.; Chen, Z.; Chen, J.; Zhou, Y. A batch sliding window method for local singularity mapping and its application for geochemical anomaly identification. *Comput. Geosci.* **2016**, *90*, 189–201. [CrossRef]
27. Wang, Z.; Cheng, Q. Characterization of micro-texture of quartz mylonite deformation process using fractal P–A model. *Earth Sci.-J. China U. Geosci.* **2006**, *31*, 361–365.
28. Wang, Z.; Cheng, Q.; Cao, L.; Xia, Q.; Chen, Z. Fractal modelling of the microstructure property of quartz mylonite during deformation process. *Math. Geol.* **2007**, *39*, 53–68. [CrossRef]
29. Wang, Z.; Cheng, Q.; Xu, D.; Dong, Y. Fractal modeling of sphalerite banding in Jinding Pb-Zn deposit, Yunnan, southwestern China. *J. China U. Geosci.* **2008**, *19*, 77–84.
30. Peterzell, M.; Kruhl, J.H. Automation of pattern recognition and fractal-geometry-based pattern quantification, exemplified by mineral-phase distribution patterns in igneous rocks. *Comput. Geosci.* **2009**, *35*, 1415–1426. [CrossRef]
31. Golsanami, N.; Fernando, S.G.; Jayasuriya, M.N.; Yan, W.; Dong, H.; Cui, L.; Dong, X.; Barzgar, E. Fractal properties of various clay minerals obtained from SEM images. *Geofluids* **2021**, *2021*, 5516444. [CrossRef]
32. Yu, C.; Liu, J. Fractal and multifractal analyses of sphalerite banding at the Zhaishang gold deposit, western Qinling, China. *Eur. J. Mineral.* **2015**, *27*, 511–520. [CrossRef]
33. Dinç Göğüş, Ö.; Avşar, E.; Develi, K.; Çalık, A. Quantifying the Rock Damage Intensity Controlled by Mineral Compositions: Insights from Fractal Analyses. *Fractal Fract.* **2023**, *7*, 383. [CrossRef]
34. Xu, D.; Ke, X.; Xie, S.; Cheng, Q. Scaling properties of feldspar and quartz in micro-images of ideal granites. *J. China U. Geosci.* **2008**, *19*, 327–333.
35. Xie, S.; Cheng, Q.; Li, Z.; Xing, X.; Chen, S. Assessing Microstructures of Ore-minerals by multifractal. *Earth Sci.-J. China U. Geosci.* **2009**, *34*, 263–269. (In Chinese with English abstract)
36. Bommasani, R.; Hudson, D.A.; Adeli, E.; Altman, R.; Arora, S.; von Arx, S.; Bernstein, M.S.; Bohg, J.; Bosselut, A.; Brunskill, E.; et al. On the opportunities and risks of foundation models. *arXiv* **2021**, arXiv:2108.07258.
37. OpenAI. ChatGPT. Available online: <https://openai.com/blog/chatgpt/> (accessed on 15 December 2023).
38. Brown, T.; Mann, B.; Ryder, N.; Subbiah, M.; Kaplan, J.D.; Dhariwal, P.; Neelakantan, A.; Shyam, P.; Sastry, G.; Askell, A.; et al. Language models are few-shot learners. *Adv. Neural Inf. Process. Syst.* **2020**, *33*, 1877–1901.
39. Kirillov, A.; Mintun, E.; Ravi, N.; Mao, H.; Rolland, C.; Gustafson, L.; Xiao, T.; Whitehead, S.; Berg, A.C.; Lo, W.-Y.; et al. Segment anything. *arXiv* **2023**, arXiv:2304.02643.
40. Chen, F.; Chen, L.; Han, H.; Zhang, S.; Zhang, D.; Liao, H. The ability of Segmenting Anything Model (SAM) to segment ultrasound images. *Biosci. Trends* **2023**, *17*, 211–218. [CrossRef]

41. Yin, L.; Zhu, J.; Hu, S. Multiple-staged granite evolution and Ta-Nb mineralization in South China. *J. Asian Earth Sci.* **1993**, *8*, 321–328.
42. Yin, L.; Pollard, P.J.; Hu, S.; Taylor, R.G. Geologic and geochemical characteristics of the Yichun Ta-Nb-Li deposit, Jiangxi Province, South China. *Econ. Geol.* **1995**, *90*, 577–585. [[CrossRef](#)]
43. Pollard, P.J. The Yichun Ta-Sn-Li deposit, South China: Evidence for extreme chemical fractionation in F-Li-P-rich magma. *Econ. Geol.* **2021**, *116*, 453–469. [[CrossRef](#)]
44. Wu, M.; Samson, I.M.; Zhang, D. Textural features and chemical evolution in Ta-Nb oxides: Implications for deuteric rare-metal mineralization in the Yichun granite-marginal pegmatite, southeastern China. *Econ. Geol.* **2018**, *113*, 937–960. [[CrossRef](#)]
45. Li, J.; Huang, X.; He, P.; Li, W.; Yu, Y.; Chen, L. In situ analyses of micas in the Yashan granite, South China: Constraints on magmatic and hydrothermal evolutions of W and Ta–Nb bearing granites. *Ore Geol. Rev.* **2015**, *65*, 793–810. [[CrossRef](#)]
46. Huang, X.; Wang, R.; Chen, X.; Hu, H.; Liu, C. Vertical variations in the mineralogy of the Yichun topaz–lepidolite granite, Jiangxi Province, southern China. *Can. Mineral.* **2002**, *40*, 1047–1068. [[CrossRef](#)]
47. Ning, G.; Liang, H.; Jiang, Z.; Zhang, H.; Liao, H. The potential of ‘Segment Anything’ (SAM) for universal intelligent ultrasound image guidance. *Biosci. Trends* **2023**, *17*, 230–233. [[CrossRef](#)]
48. Meta AI. Segment Anything. Available online: <https://segment-anything.com> (accessed on 15 December 2023).
49. Psychogyios, K.; Leligou, H.C.; Melissari, F.; Bourou, S.; Anastasakis, Z.; Zahariadis, T. SAMStyler: Enhancing Visual Creativity with Neural Style Transfer and Segment Anything Model (SAM). *IEEE Access* **2023**, *11*, 100256–100267. [[CrossRef](#)]
50. Dosovitskiy, A.; Beyer, L.; Kolesnikov, A.; Weissenborn, D.; Zhai, X.; Unterthiner, T.; Dehghani, M.; Minderer, M.; Heigold, G.; Gelly, S.; et al. An image is worth 16x16 words: Transformers for image recognition at scale. *arXiv* **2020**, arXiv:2010.11929.
51. He, K.; Chen, X.; Xie, S.; Li, Y.; Dollár, P.; Girshick, R. Masked autoencoders are scalable vision learners. In Proceedings of the IEEE/CVF Conference on Computer Vision and Pattern Recognition, New Orleans, LA, USA, 18–24 June 2022; pp. 16000–16009.
52. Vaswani, A.; Shazeer, N.; Parmar, N.; Uszkoreit, J.; Jones, L.; Gomez, A.N.; Kaiser, Ł.; Polosukhin, I. Attention is all you need. *Adv. Neural Inf. Process. Syst.* **2017**, *30*.
53. Shi, P.; Qiu, J.; Abaxi, S.M.D.; Wei, H.; Lo, F.P.-W.; Yuan, W. Generalist vision foundation models for medical imaging: A case study of segment anything model on zero-shot medical segmentation. *Diagnostics* **2023**, *13*, 1947. [[CrossRef](#)]
54. Russell, B.C.; Torralba, A.; Murphy, K.P.; Freeman, W.T. LabelMe: A database and web-based tool for image annotation. *Int. J. Comput. Vis.* **2008**, *77*, 157–173. [[CrossRef](#)]
55. Sauvola, J.; Pietikäinen, M. Adaptive document image binarization. *Pattern Recognit.* **2000**, *33*, 225–236. [[CrossRef](#)]
56. Van Rossum, G.; Drake, F.L. *Python Reference Manual*; Centrum voor Wiskunde en Informatica: Amsterdam, Netherlands, 1995; pp. 1–52.
57. Bradski, G. The openCV library. *Dr. Dobbs. J.* **2000**, *25*, 120–123.
58. Bradski, G.; Kaehler, A. *Learning OpenCV: Computer Vision with the OpenCV Library*; O’Reilly Media, Inc.: Sebastopol, CA, USA, 2008.
59. Xie, G.; Lu, W. Image edge detection based on opencv. *Int. J. Electr. Comput. Eng.* **2013**, *1*, 104–106. [[CrossRef](#)]
60. Mandelbrot, B.B.; Frame, M. *Fractals*. In *Hasard et Finances*, 1st ed.; Flammarion: Paris, France, 1997.
61. Takayasu, H. *Fractals in the Physical Sciences*; Manchester University Press: Manchester, UK, 1990.
62. Lovejoy, S. Area-perimeter relation for rain and cloud areas. *Science* **1982**, *216*, 185–187. [[CrossRef](#)] [[PubMed](#)]
63. Lung, C.W.; Mu, Z.Q. Fractal dimension measured with perimeter-area relation and toughness of materials. *Phys. Rev. B* **1988**, *38*, 11781. [[CrossRef](#)] [[PubMed](#)]
64. Schlueter, E.M.; Zimmerman, R.W.; Witherspoon, P.A.; Cook, N.G.W. The fractal dimension of pores in sedimentary rocks and its influence on permeability. *Eng. Geol.* **1997**, *48*, 199–215. [[CrossRef](#)]
65. Salat, H.; Murcio, R.; Arcaute, E. Multifractal methodology. *Physica. A* **2017**, *473*, 467–487. [[CrossRef](#)]
66. Halsey, T.C.; Jensen, M.H.; Kadanoff, L.P.; Procaccia, I.; Shraiman, B.I. Fractal measures and their singularities: The characterization of strange sets. *Phys. Rev. A* **1986**, *33*, 1141. [[CrossRef](#)]
67. Agterberg, F.P.; Cheng, Q.; Brown, A.; Good, D. Multifractal modeling of fractures in the Lac du Bonnet batholith, Manitoba. *Comput. Geosci.* **1996**, *22*, 497–507. [[CrossRef](#)]
68. Cheng, Q. Multifractal modeling and lacunarity analysis. *Math. Geol.* **1997**, *29*, 919–932. [[CrossRef](#)]
69. Chhabra, A.B.; Meneveau, C.; Jensen, R.V.; Sreenivasan, K. Direct determination of the $f(\alpha)$ singularity spectrum and its application to fully developed turbulence. *Phys. Rev. A* **1989**, *40*, 5284. [[CrossRef](#)] [[PubMed](#)]
70. Atmanspacher, H.; Scheingraber, H.; Wiedenmann, G. Determination of $f(\alpha)$ for a limited random point set. *Phys. Rev. A* **1989**, *40*, 3954. [[CrossRef](#)] [[PubMed](#)]
71. Vázquez, E.V.; Ferreira, J.P.; Miranda, J.; González, A.P. Multifractal analysis of pore size distributions as affected by simulated rainfall. *Vadose Zone J.* **2008**, *7*, 500–511. [[CrossRef](#)]
72. Kropp, J.; Block, A.; von Bloh, W.; Klenke, T.; Schellnhuber, H. Multifractal characterization of microbially induced magnesian calcite formation in Recent tidal flat sediments. *Sediment. Geol.* **1997**, *109*, 37–51. [[CrossRef](#)]
73. Hentschel, H.G.E.; Procaccia, I. The infinite number of generalized dimensions of fractals and strange attractors. *Phys. D* **1983**, *8*, 435–444. [[CrossRef](#)]
74. Ge, X.; Fan, Y.; Li, J.; Zahid, M.A. Pore structure characterization and classification using multifractal theory—An application in Santanghu basin of western China. *J. Petrol. Sci. Eng.* **2015**, *127*, 297–304. [[CrossRef](#)]

75. Osco, L.P.; Wu, Q.; de Lemos, E.L.; Gonçalves, W.N.; Ramos, A.P.M.; Li, J.; Junior, J.M. The segment anything model (sam) for remote sensing applications: From zero to one shot. *Int. J. Appl. Earth Obs.* **2023**, *124*, 103540. [[CrossRef](#)]
76. Han, S.; Löhr, S.C.; Abbott, A.N.; Baldermann, A.; Farkaš, J.; McMahon, W.; Milliken, K.L.; Rafiei, M.; Wheeler, C.; Owen, M. Earth system science applications of next-generation SEM-EDS automated mineral mapping. *Front. Earth Sci.* **2022**, *10*, 956912. [[CrossRef](#)]
77. Xue, D.; Zhou, H.; Ren, W.; Zhao, B. Multi-fractal characteristics of joint geometric distribution of granite in Beishan. *Rock Soil Mech.* **2016**, *37*, 2937–2944.
78. Zhou, Z.; Zhang, S.; Gao, Z.; Cai, X.; Li, H. Multifractal characterization of gangue particle size distribution structure during ball milling process. *Powder Technol.* **2022**, *412*, 117970. [[CrossRef](#)]
79. Izadi, H.; Sadri, J.; Bayati, M. An intelligent system for mineral identification in thin sections based on a cascade approach. *Comput. Geosci.-UK* **2017**, *99*, 37–49. [[CrossRef](#)]
80. Lou, W.; Zhang, D.; Bayless, R.C. Review of mineral recognition and its future. *Appl. Geochem.* **2020**, *122*, 104727. [[CrossRef](#)]
81. Gao, Q.; Long, T.; Zhou, Z. Mineral identification based on natural feature-oriented image processing and multi-label image classification. *Expert Syst. Appl.* **2024**, *238*, 122111. [[CrossRef](#)]
82. Gulbin, Y.; Evangulova, E. Morphometry of quartz aggregates in granites: Fractal images referring to nucleation and growth processes. *Math. Geol.* **2003**, *35*, 819–833. [[CrossRef](#)]
83. Fowler, A.D. Self-organized mineral textures of igneous rocks: The fractal approach. *Earth-Sci. Rev.* **1990**, *29*, 47–55. [[CrossRef](#)]
84. Xie, Y.; Tan, K.; Wang, Z.; Hu, K. An Numerical Approach for the Dynamic Model of Fractal Growth of Minerals. *J. U. Souty Chin.* **2011**, *25*, 33–36. (In Chinese with English abstract)
85. Witten, T.A., Jr.; Sander, L.M. Diffusion-limited aggregation, a kinetic critical phenomenon. *Phys. Rev. Lett.* **1981**, *47*, 1400. [[CrossRef](#)]
86. Tokuyama, M.; Kawasaki, K. Fractal dimensions for diffusion-limited aggregation. *Phys. Lett. A* **1984**, *100*, 337–340. [[CrossRef](#)]
87. Schwartz, M. Geochemical criteria for distinguishing magmatic and metasomatic albite-enrichment in granitoids—Examples from the Ta-Li granite Yichun (China) and the Sn-W deposit Tikus (Indonesia). *Miner. Depos.* **1992**, *27*, 101–108. [[CrossRef](#)]
88. Abuamarah, B.A.; Azer, M.K.; Asimow, P.D.; Shi, Q. Petrogenesis of the post-collisional rare-metal-bearing Ad-Dayheen granite intrusion, Central Arabian Shield. *Lithos* **2021**, *384*, 105956. [[CrossRef](#)]
89. Moussa, H.E.; Asimow, P.D.; Azer, M.K.; Abou El Maaty, M.A.; Akarish, A.I.; Yanni, N.N.; Mubarak, H.S.; Wilner, M.; Elsagheer, M.A. Magmatic and hydrothermal evolution of highly-fractionated rare-metal granites at Gabal Nuweibi, Eastern Desert, Egypt. *Lithos* **2021**, *400*, 106405. [[CrossRef](#)]
90. Gahlan, H.A.; Azer, M.K.; Al-Hashim, M.H.; Heikal, M.T.S. Highly evolved rare-metal bearing granite overprinted by alkali metasomatism in the Arabian Shield: A case study from the Jabal Tawlah granites. *J. Afr. Earth Sci.* **2022**, *192*, 104556. [[CrossRef](#)]
91. Sami, M.; El Monsef, M.A.; Abart, R.; Toksoy-Köksal, F.; Abdelfadil, K.M. Unraveling the Genesis of Highly Fractionated Rare-Metal Granites in the Nubian Shield via the Rare-Earth Elements Tetrad Effect, Sr–Nd Isotope Systematics, and Mineral Chemistry. *ACS Earth Space Chem.* **2022**, *6*, 2368–2384. [[CrossRef](#)]
92. Wang, C. A Discussion on Genesis of the 414 Deposit. *Miner. Depos.* **1986**, *2*, 85–96. (In Chinese)
93. Rong, J.; Wang, F. *Metasomatic Textures in Granites: Evidence from Petrographic Observation*; Springer: Singapore, 2016; pp. 69–98.

Disclaimer/Publisher’s Note: The statements, opinions and data contained in all publications are solely those of the individual author(s) and contributor(s) and not of MDPI and/or the editor(s). MDPI and/or the editor(s) disclaim responsibility for any injury to people or property resulting from any ideas, methods, instructions or products referred to in the content.